iScience

CellPress

Article

Asymmetrical 3D Nanoceria Channel for Severe Neurological Defect Regeneration

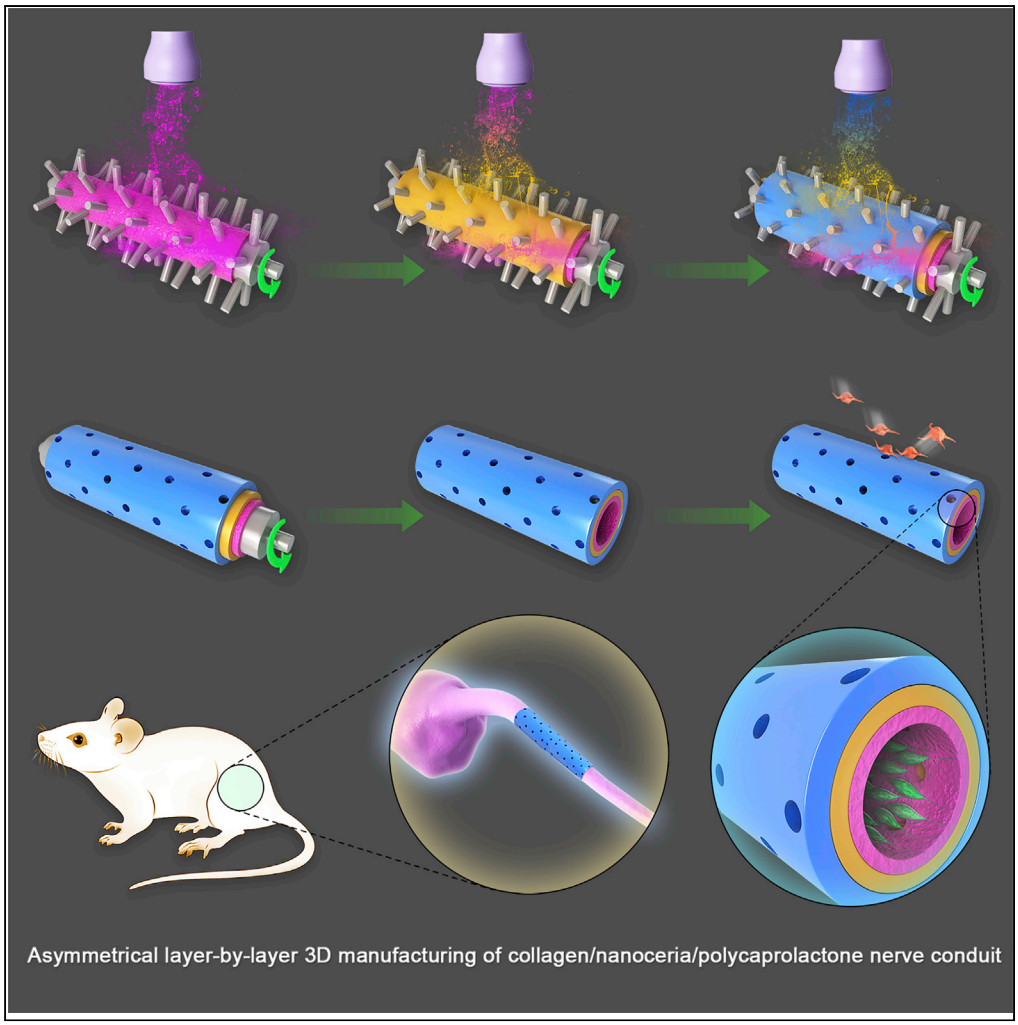

Yun Qian, Qixin Han, Xiaotian Zhao, Hui Li, Wei-En Yuan, Cunyi Fan

yuanweien@sjtu.edu.cn (W.-E.Y.)
cyfan@sjtu.edu.cn (C.F.)

HIGHLIGHTS

Collagen/nanoceria/polycaprolactone conduit was prepared by asymmetrical fabrication

The scaffold induced proliferation, adhesion, and angiogenesis in nerve repair

The scaffold alleviated oxidative stress and inflammation in the microenvironment

Qian et al., iScience *12*, 216–231
February 22, 2019
https://doi.org/10.1016/j.isci.2019.01.013

iScience

CellPress

Article

Asymmetrical 3D Nanoceria Channel for Severe Neurological Defect Regeneration

Yun Qian,[1] Qixin Han,[2,5] Xiaotian Zhao,[3] Hui Li,[4] Wei-En Yuan,[3,6,*] and Cunyi Fan[1,*]

SUMMARY

Inflammation and oxidative stress are major problems in peripheral nerve injury. Nanoceria can manipulate antioxidant factor expression, stimulate angiogenesis, and assist in axonal regeneration. We fabricate collagen/nanoceria/polycaprolactone (COL/NC/PCL) conduit by asymmetrical three-dimensional manufacture and find that this scaffold successfully improves Schwann cell proliferation, adhesion, and neural expression. In a 15-mm rat sciatic nerve defect model, we further confirm that the COL/NC/PCL conduit markedly alleviates inflammation and oxidative stress, improves microvessel growth, and contributes to functional, electrophysiological, and morphological nerve restoration in the long term. Our findings provide compelling evidence for future research in antioxidant nerve conduit for severe neurological defects.

INTRODUCTION

Wallerian degeneration (WD) occurs at the beginning of acute peripheral nerve injury (PNI), accompanied by recruitment of macrophages. The communication between Schwann cells and macrophages helps to clear myelin debris and to initiate axon growth in the early phase of PNI. Inflammation is a double-edged sword for nerve regeneration. Contradictory effects are associated with the timing of inflammatory process in severe nerve injury. After the early phase of WD, macrophages continue to express pro-inflammatory cues that lead to the transcription of reactive oxygen species (ROS) and activation of secondary cascade of events. These events include hemorrhage, edema, inflammation via inhibition of blood flow, and release of anti-regenerative substances. The consequent effects result in the activation of the cell death machinery and compromise of the neural regeneration process.

Bioactive nerve conduit should effectively repair nerve injury by inhibiting oxidative stress and inflammation. Melatonin-based polycaprolactone nerve conduit reduced oxidative stress and inflammation in lengthy sciatic nerve defects. In addition, it alleviated Schwann cell apoptosis by mediating autophagy-related signaling (Qian et al., 2018a). Poly(D,L-lactic acid)/poly(lactic acid)-co-(glycolic acid)-alt-(L-lysine)/β-tricalcium phosphate (PDLLA/PRGD/β-TCP) conduits can regulate neurotrophin excretion into the microenvironment and reduce the oxidative stress in sciatic nerve regeneration (Qiu et al., 2014). PRGD/PDLLA capping conduit defeated inflammatory infiltration and hazardous collagen deposition as a physical barrier (Yi et al., 2018). Green synthesis of cerium oxide nanoparticle (nanoceria) has aroused interest in nontoxic nanoparticle application for tissue engineering. Nanoceria have two oxide states, Ce^{3+} (reduced) and Ce^{4+} (oxidized) on the surface. The state is changed by external stimulation and causes switch-on and switch-off for the catalytic antioxidant potential via oxidation and deoxidation. Nanoceria acts as a superoxide dismutase or catalase (CAT) mimetic when surface Ce^{3+} is at a high concentration. Exposure of pancreas to diazinon leads to significant oxidative stress. Nanoceria administration can reduce apoptosis of islets, reduce blood sugar level, and control weight loss and thus inhibit oxidative stress (Khaksar et al., 2017). Nanoceria has also significantly restored muscle strength and extended life expectancy in amyotrophic lateral sclerosis study via the increased CAT and oxidase activities (DeCoteau et al., 2016). Apart from the high antioxidant potential, it also has excellent biocompatibility, regenerative capacity, high stability, low cost of synthesis, and ease of storage. In the nervous system, nanoceria is considered to exert positive effects on nerve regeneration after acute or chronic oxidant insult (Najafi et al., 2017). Nanoceria had no adverse effects on the viability of PC12 cells. Instead, it improved neuronal differentiation by extending neurite length (Ciofani et al., 2013). Nanoceria modified with the functional group of polyacrylic acid alleviated H_2O_2-induced oxidative stress in PC12 cells by regulating cleaved caspase-3 and mitochondrial cytochrome *c* in the apoptosis-related pathways (Jia et al., 2018). Ceria/polyoxometalate hybrid can degrade amyloid-β aggregates, reduce intracellular ROS, and deactivate microglial cells, which leads to decreased neurotoxicity (Guan et al., 2016). Nanoceria/gelatin scaffolds fabricated by electrospinning display strong

[1]Department of Orthopedics, Shanghai Jiao Tong University Affiliated Sixth People's Hospital, Shanghai 200233, China

[2]Center for Reproductive Medicine, Renji Hospital, School of Medicine, Shanghai Jiao Tong University, Shanghai 200135, China

[3]Engineering Research Center of Cell & Therapeutic Antibody, Ministry of Education, School of Pharmacy, Shanghai Jiao Tong University, Shanghai 200240, China

[4]School of Medicine, University of California, 1450 Third St., San Francisco, CA 94158, USA

[5]Shanghai Key Laboratory for Assisted Reproduction and Reproductive Genetics, Shanghai 200135, China

[6]Lead Contact

*Correspondence: yuanweien@sjtu.edu.cn (W.-E.Y.), cyfan@sjtu.edu.cn (C.F.)

https://doi.org/10.1016/j.isci.2019.01.013

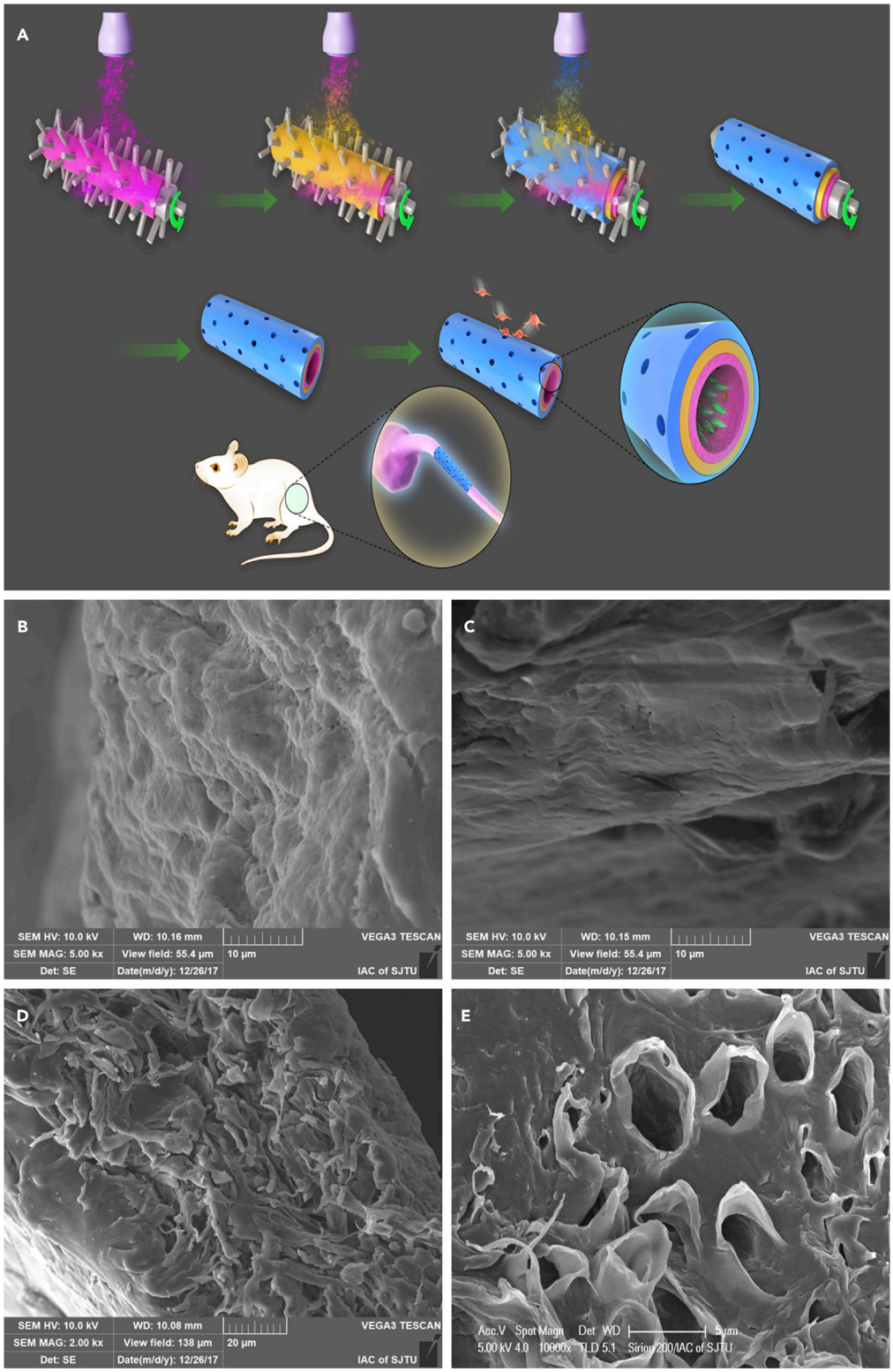

Figure 1. Schematic Illustration of COL/NC/PCL Nerve Conduit Fabrication and Implantation into a Rat Model

(A) Asymmetrical three-dimensional layer-by-layer manufacture of COL/NC/PCL nerve conduit. It was composed of three layers: the innermost NC/PCL mixed layer, the outermost COL layer, and the middle PCL layer. A tube mold was rolling counterclockwise, under a sprayer that injected different solutions layer by layer on the rolling tube. A microneedle on the

Figure 1. *Continued*
tube assured even pore size that allowed free exchanges of nutrients into the conduit. The schematic illustration showed Schwann cell adhesion to the innermost layer and fibroblast detachment from the outermost layer.
(B) Rough innermost layer; scale bar, 10 μm.
(C) Smooth outermost layer; scale bar, 10 μm.
(D) Multilayered structure and an increasing gradient change in roughness inside out; scale bar, 20 μm.
(E) Microporous structure in the COL/NC/PCL nerve conduit; scale bar, 5 μm.

ROS capacity, slow the cell aging, and improve neurite sprouting (Marino et al., 2017). However, nanoceria was also reported to pose hazard to the neural stem cells by inhibiting their differentiation and interfering with the cytoskeletal organization (Gliga et al., 2017). In previous findings, nanoceria displays better antioxidant potential in clearing ROS and restoring immune balance. However, the cytotoxicity for neurons is questionable. Therefore, in this study, we will further explore the cytotoxicity, antioxidant, and regenerative functions of nanoceria in nerve tissue engineering, especially for severe nerve defects.

RESULTS AND DISCUSSION

Three-Dimensional Asymmetrical Manufacture of COL/NC/PCL Nerve Conduit

In this study, we fabricated a collagen/nanoceria/polycaprolactone (COL/NC/PCL) nerve conduit via asymmetrical layer-by-layer 3D manufacture. The conduit was composed of three layers: the innermost NC/PCL mixed layer, the outermost COL layer, and the middle PCL layer. A tube mold was rolling counterclockwise, under a sprayer that injected different solutions layer by layer on the rolling tube. A microneedle on the tube assured even pore size, which allowed free exchanges of nutrients into the conduit. Microstructured PCL filaments can increase bands of Büngner and improve nerve regeneration (Carrier-Ruiz et al., 2015). We fabricated PCL layer and NC/PCL layer via 3D manufacture, which added to its granular sensation on the surface. In addition, PCL in 3D structure can significantly improve cell attachment, proliferation, and differentiation (Rasekh et al., 2013; Sharifi et al., 2016). The adhesive effect was further enhanced by the micro/nanosurface structure of NC/PCL topography in the innermost layer. Schwann cells can adhere firmly to the inner conduit and secrete neurotrophic factors to facilitate axonal regrowth and remyelination. An agarose/collagen composite sheet can prevent adhesion of mesenchymal cells and extracellular matrix (ECM) on the lesion tissues (Tang et al., 2007). Hyaluronic acid and collagen can be fabricated as a spongy sheet to stop peritoneal adhesion to peripheral organs (Kuroyanagi et al., 2014). The dense outermost collagen layer prevented tissue adhesion in the surroundings. Therefore, we developed an adhesion gradient from the innermost to the outermost layer, supported by asymmetrical layer-by-layer 3D manufacture technique (Figure 1).

Mechanical and Structural Characteristics of the COL/NC/PCL Conduit

We characterized the COL/NC/PCL nerve conduit via scanning electron microscopy (SEM). The innermost layer was significantly rougher than the outermost layer. The cross-sectional view showed multilayered structure and an increasing gradient change in roughness inside out (Figure 1). We also observed NC morphology and distribution in the scaffold using transmission electron microscopy (TEM) and SEM, respectively. The cerium oxide nanoparticles were relatively evenly distributed in the scaffold and were around 10–50 nm in diameter (Figure S1). Also, they displayed excellent antioxidant properties. The antioxidant activity of 1 mg nanoceria corresponds to that of 100 nmol Trolox. We evaluated the mechanical properties, including conduit thickness and elastic modulus, and found that the COL/NC/PCL conduit was thicker, softer, and less elastic than the NC/PCL conduit, owing to collagen application (Figure S2). Both conduits displayed good elasticity that could support long-term *in vivo* nerve regeneration, free from conduit collapse. In the fabrication course, microneedles on the mold facilitated microporous architecture, which introduced free exchanges of nutrients, water, and other macromolecules into the conduit lumen (Figure 1; Qian et al., 2018b).

Excellent Biocompatibility of COL/NC/PCL Conduit for RSCs

We assessed the biocompatibility of COL/NC/PCL and NC/PCL conduits to determine their appropriate concentration for neural growth, from 0.5%, 1%, 2% to 4% nanoceria in different conduits using cell counting kit 8 (CCK8) assay. It showed that 1% nanoceria was much less cytotoxic than 2% and 4% and was slightly more toxic than the 0.5% counterpart after 24 h (Figure S3). This was consistent with a previous finding that 1 $\mu g\ mL^{-1}$ nanoceria was the optimal concentration of biological effectiveness for hippocampal neurons (Estevez et al., 2011). We further used 1% nanoceria in the following experiments.

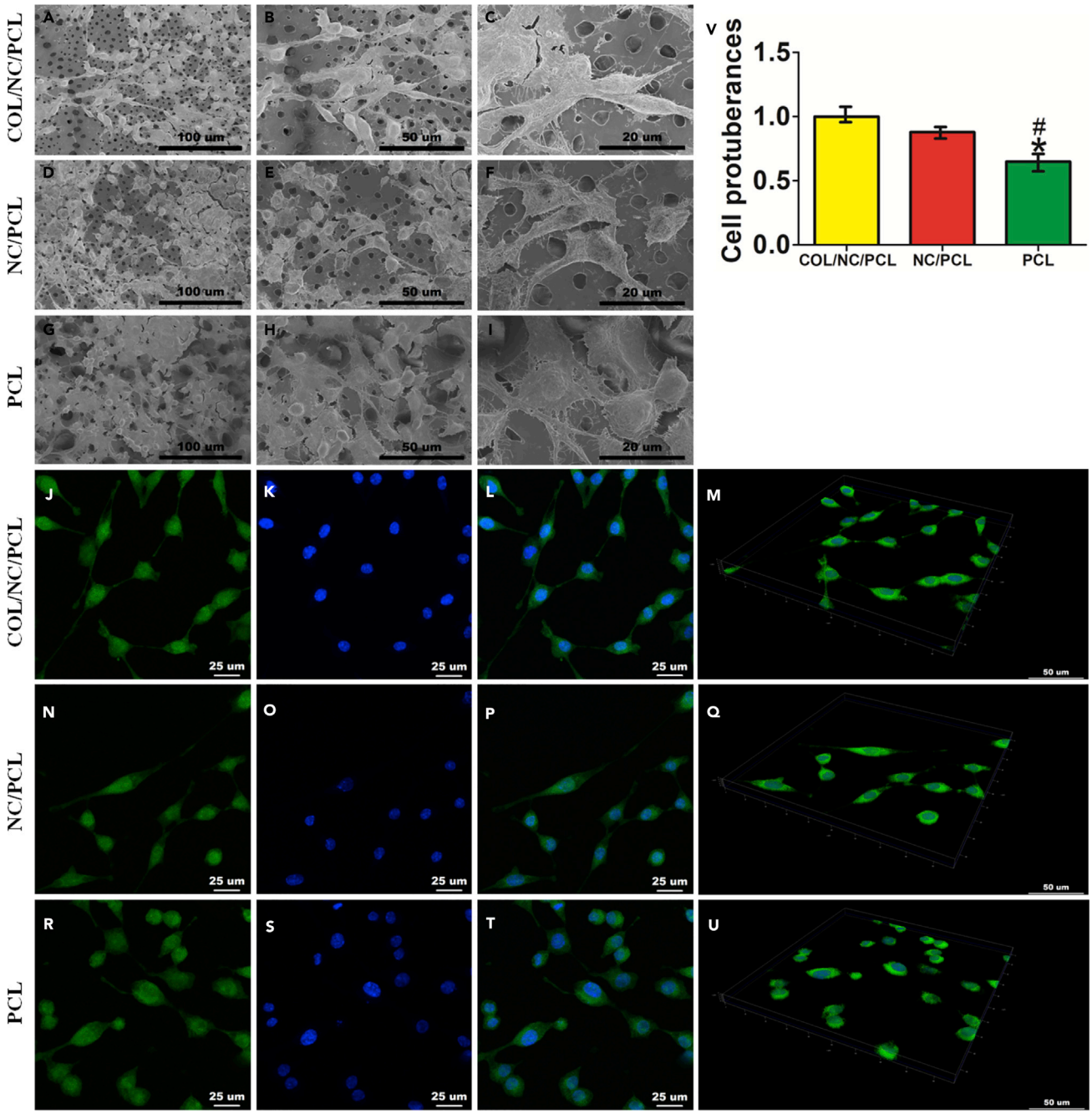

Figure 2. Schwann Cell Morphology in Different Conduits

(A–U) Cell morphology in different nerve conduits evaluated by SEM (A–I) and immunofluorescence (J–U).

(A–C) Cell morphology in COL/NC/PCL conduit.

(D–F) Cell morphology in NC/PCL conduit.

(G–I) Cell morphology in PCL conduit. Scale bars, 100 μm in (A, D, and G); 50 μm in (B, E, and H); and 20 μm in (C, F, and I).

(J–M) Phalloidin staining showing cell attachment in COL/NC/PCL conduit.

(J, N, and R) Phalloidin staining; scale bars, 25 μm.

(K, O, and S) DAPI staining; scale bars, 25 μm.

(L, P, and T) Merged images; scale bars, 25 μm.

(M, Q, and U) 3D display for cell attachment in different conduits; scale bars, 50 μm.

(V) Cell protuberances in different conduits, *$p < 0.05$ compared with COL/NC/PCL, $^{\#}p < 0.05$ compared with NC/PCL.

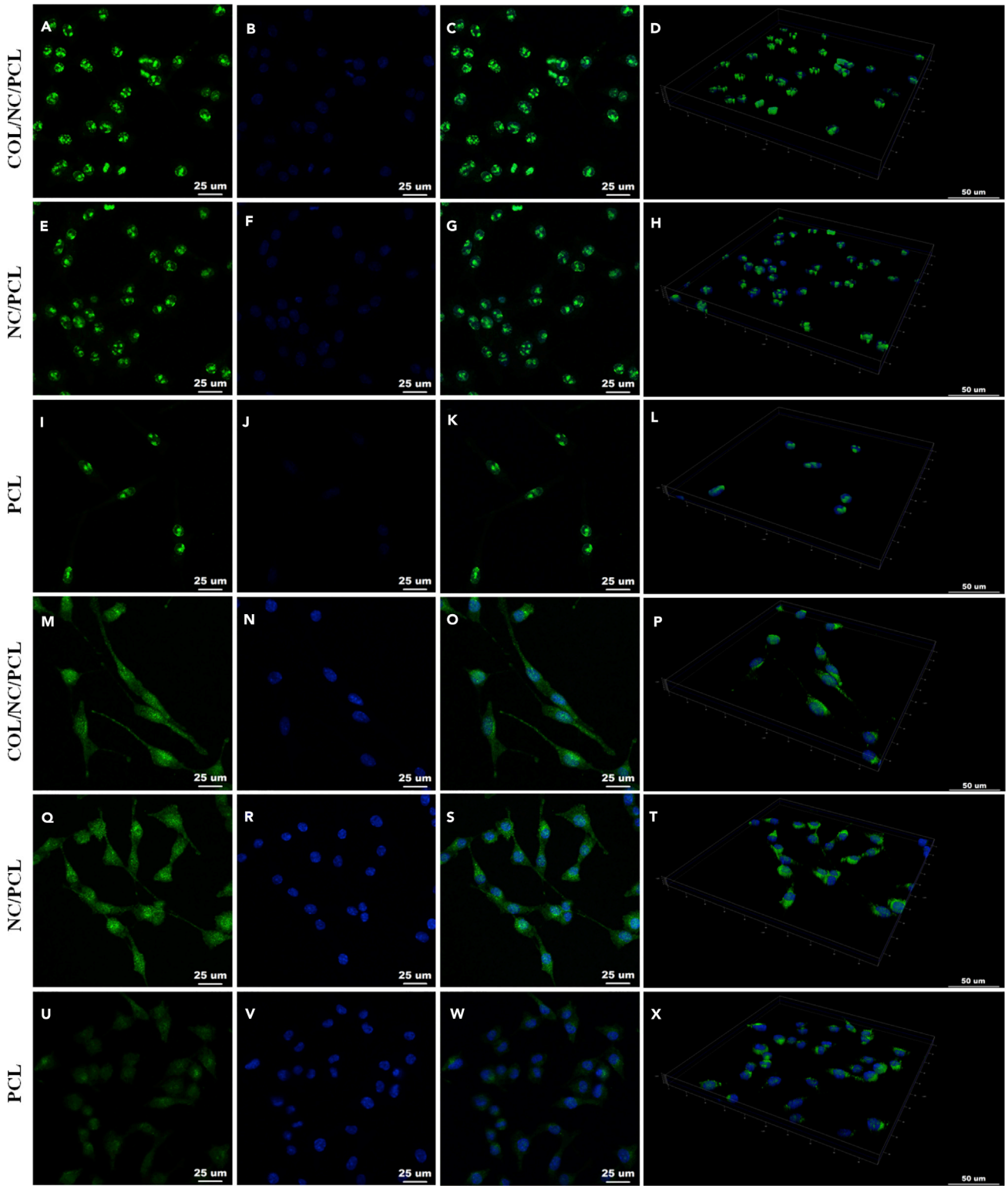

Figure 3. Immunofluorescence of Ki67 and GFAP

(A–D) Ki67 expression in COL/NC/PCL.

(E–H) Ki67 expression in NC/PCL.

(I–L) Ki67 expression in PCL.

Figure 3. *Continued*
(M–P) GFAP expression in COL/NC/PCL.
(Q–T) GFAP expression in NC/PCL.
(U–X) GFAP expression in PCL.
(A, E, and I) Ki67 staining; scale bars, 25 μm.
(M, Q, and U) GFAP staining; scale bars, 25 μm.
(B, F, J, N, R, and V) DAPI staining; scale bars, 25 μm.
(C, G, K, O, S, and W) Merged images; scale bars, 25 μm.
(D, H, L, P, T, and X) 3D display; scale bars, 50 μm. GFAP, glial fibrillary acidic protein.

Firm Attachment and Neural Expression of RSCs on the COL/NC/PCL Conduit

We observed rat Schwann cell (RSC) morphology in different conduits. Cell protuberances were more extended in COL/NC/PCL conduit than in the NC/PCL and PCL counterparts (Figure 2). Excellent cellular adhesion and elongation was supported by tensile stresses originating from the micro- and nanostructured pores in the conduit (Marino et al., 2013). Cell proliferation assay was performed using CCK8 at 24, 72, 120, and 168 h, showing that COL/NC/PCL and NC/PCL conduits improved cell growth compared with the PCL counterpart. We also evaluated Ki67 expression of cells from different conduits. It also showed a higher expression from COL/NC/PCL and NC/PCL conduits than the PCL counterpart ($p < 0.05$, Figure 3).

Nanoceria can regulate neuronal cell fate. It promoted neuronal repair by regulating brain-derived neurotrophic factor signaling in Alzheimer disease (D'Angelo et al., 2009). It also improved neurogenesis by ameliorating hypoxia-dependent memory loss (Arya et al., 2016). In this study, we evaluated the neural expression of RSCs in COL/NC/PCL conduit. The axonal orientation and myelination states were evaluated by S100, β-III-tubulin (Tuj1), myelin basic protein (MBP), and glial fibrillary acidic protein (GFAP) expression *in vitro* (Figures 3, 4, and 5). Their expression from COL/NC/PCL conduit was similar to NC/PCL and significantly higher than the PCL counterpart ($p<0.05$) confirmed by immunofluorescent assay. Moreover, we also performed western blot (WB) and quantitative PCR (qPCR) to revalidate our findings *in vitro* (Figure 5).

Antioxidant and Anti-inflammatory Roles of COL/NC/PCL Conduit

In addition to neural protection, the ability of nanoceria to scavenge oxidative stress is very significant for the oxygen-enriched organs and systems. Different manufacturing techniques contributed to nanoceria fabrication with the unique capability of oxygen storage, release, and clearance (Ishikawa et al., 2016; Yao et al., 2018). Nanoceria reduced ROS production and DNA and protein damages to repair and restore main cell activities in cardiac engineering (Pagliari et al., 2012). Water-soluble nanoceria could scavenge ROS and accumulative oxidative insult in age-associated macular diseases (Mitra et al., 2017). In the presence of a H_2O_2 oxidant insult, we performed 2′,7′-dichlorofluorescein diacetate (DCFDA) flow cytometry assay and evaluated some antioxidant and inflammatory markers' expression, such as hemeoxygenase 1 (HO-1), manganese-dependent superoxide dismutase (MnSOD) , glutamate-cysteine ligase catalytic (GCLC), and interleukin 6 (IL-6), using WB and qPCR assays. The oxidative stress state in cells cultured in COL/NC/PCL and NC/PCL conduits was significantly lower than that in PCL counterpart, indicating that nanoceria could reduce the oxidative level by scavenging ROS (Figure S4). The effect was further enhanced by collagen addition.

Nanoceria has diverse sizes varying from a few to hundreds of nanometers. Larger nanoceria was found to scavenge intracellular ROS to a greater extent than the smaller nanoceria, and ROS scavenging was found to increase with treatment time (Vassie et al., 2017). In this study, we purchased 20-nm-diameter nanoceria, which improved its antioxidative stress ability.

In Vivo Regenerative Capacity of COL/NC/PCL Conduit

The antioxidant and neural protective role of nanoceria-based conduit was further evaluated in Sprague Dawley (SD) rat sciatic nerve injury model. We included COL/NC/PCL conduit, NC/PCL conduit, PCL conduit, and autograft and assessed their performances in peripheral nerve regeneration at 6, 12, and 18 weeks after surgery. We did not notice ulcer, delayed wound healing, or severe infection at each time point. Walking track analysis and withdrawal latency measurement were adopted for locomotor and sensory performance evaluation. The sciatic function index was the highest in autograft, and the results were better in COL/NC/PCL and NC/PCL conduits than the PCL counterpart at 6 and 12 weeks after surgery. At 18 weeks, the value of COL/NC/PCL conduit was similar to that of autograft, and higher than those of the others ($p<0.05$). As for withdrawal latency, the reaction time was prolonged evidently in

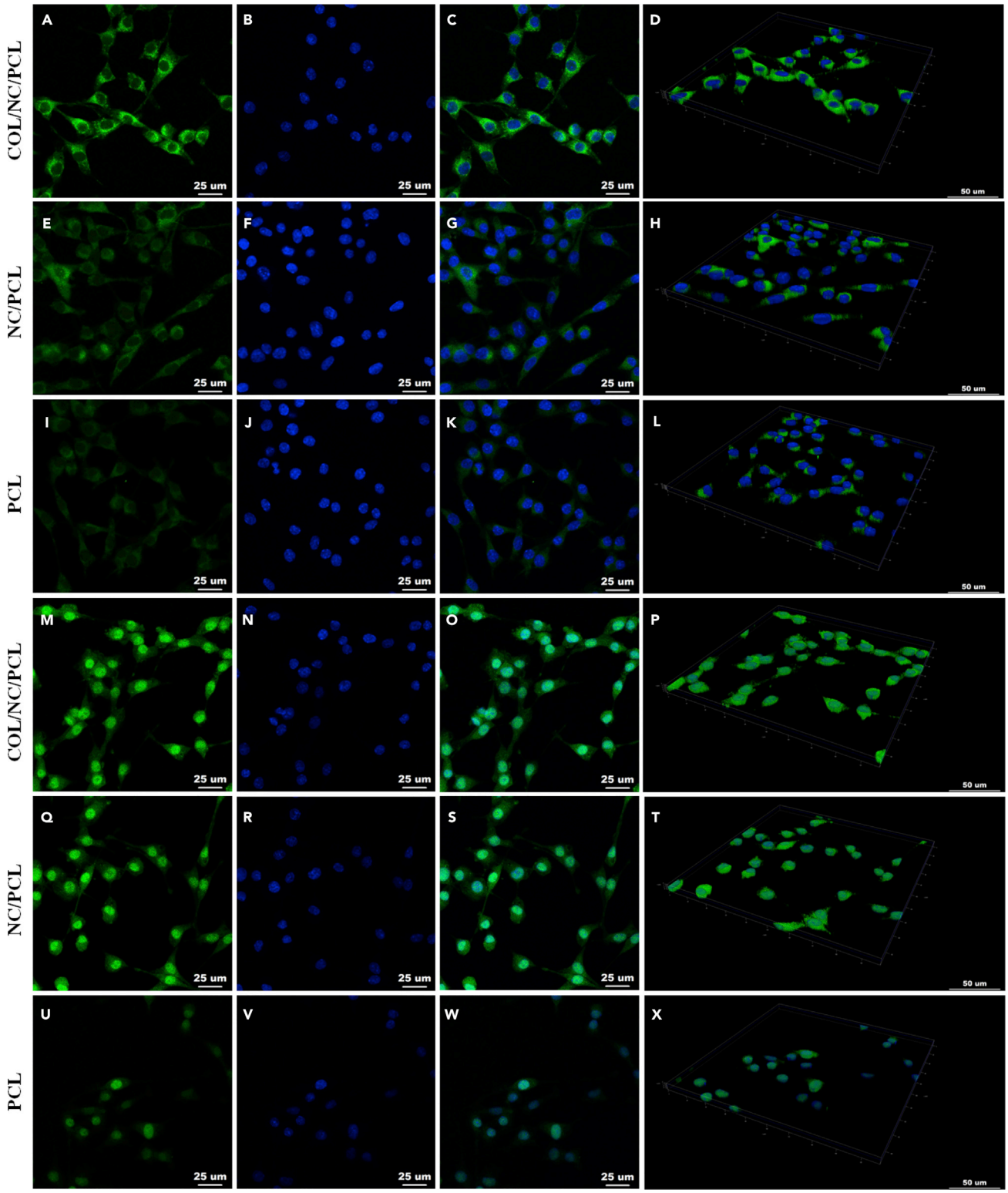

Figure 4. Immunofluorescence of S100 and Tuj1

(A–D) S100 expression in COL/NC/PCL.

(E–H) S100 expression in NC/PCL.

(I–L) S100 expression in PCL.

Figure 4. *Continued*
(M–P) Tuj1 expression in COL/NC/PCL.
(Q–T) Tuj1 expression in NC/PCL.
(U–X) Tuj1 expression in PCL.
(A, E, and I) S100 staining; scale bars, 25 μm.
(M, Q, and U) Tuj1 staining; scale bars, 25 μm.
(B, F, J, N, R, and V) DAPI staining; scale bars, 25 μm.
(C, G, K, O, S, and W) Merged images; scale bars, 25 μm.
(D, H, L, P, T, and X) 3D display, scale bars, 50 μm.

COL/NC/PCL, NC/PCL, and PCL conduits when compared with the autograft at 6 and 12 weeks after surgery. At 18 weeks, the reaction time of COL/NC/PCL conduit was still longer than that of the autograft but much shorter than that of the rest ($p < 0.05$) (Figure S5). It showed that the COL/NC/PCL conduit promoted locomotor and sensory recovery to a certain extent after severe traumatic injury.

Operated nerves were dissected from rats and subjected to electromyography testing, such as nerve conducting velocity (NCV) and distal compound motor action potential (DCMAP) (Kerasnoudis et al., 2014; Yarar et al., 2015). At 6 and 12 weeks after surgery, the NCV of COL/NC/PCL conduit (13.6 m s^{-1}, 20.4 m s^{-1}) was significantly higher than that of NC/PCL (10.1 m s^{-1}, 15.2 m s^{-1}) and PCL (7.3 m s^{-1}, 11.8 m s^{-1}) counterparts, but was still lower than that of the autograft (16.6 m s^{-1}, 25.9 m s^{-1}). Nevertheless, there was a slight difference between the COL/NC/PCL conduit (32.1 m s^{-1}) and autograft (34.7 m s^{-1}) at 18 weeks. However, the results were much better than those of the NC/PCL (25.8 m s^{-1}) and PCL (19.5 m s^{-1}) conduits. DCMAP is the total action potential of every motor endplate and an important indicator for muscle contraction gain. Like NCV, autograft outnumbered other groups in DCMAP at 6 and 12 weeks after surgery ($p < 0.05$). However, the DCMAP value of the COL/NC/PCL conduit was close to that of the autograft at 18 weeks and evidently higher that of the rest ($p < 0.05$, Figure S5). It indicated that the COL/NC/PCL conduit significantly elevated electrophysiological performance and restored electrical transduction.

After functional and electrophysiological evaluation, we prepared semithin sections from the middle portion of 15-mm regenerated nerve samples in each group and performed hematoxylin and eosin (H&E) staining, 1% toluidine blue (TB) staining, and TEM. We evaluated several indicators for peripheral nerve regeneration, such as the number of myelinated axons, thickness of myelin sheath, regenerated axon area, and average myelinated axon diameter (Qian et al., 2018c). H&E and TB staining showed that the total axon number and area results were similar between COL/NC/PCL and NC/PCL at 6 weeks. However, the diameter and thickness of regenerated nerves and myelinated axons of COL/NC/PCL conduit were higher than those of the remaining conduits at 6 and 12 weeks after surgery ($p < 0.05$, Figures S6–S8). None of them could match the results of autograft. However, at 18 weeks, COL/NC/PCL conduit and autograft showed similar values and were significantly better than NC/PCL and PCL conduits ($p < 0.05$, Figure S9). By TEM observation, the thickness and average diameter of myelinated fibers were evaluated. In COL/NC/PCL conduit, the average myelinated axon diameter and myelin thickness were evidently increased when compared with the NC/PCL and PCL counterparts ($p<0.05$) at three time points, but were lower than those in autograft at 6 and 12 weeks (Figures S10 and S11). However, no significant difference was observed between the COL/NC/PCL conduit and autograft at 18 weeks ($p > 0.05$, Figure 6).

COL/NC/PCL Alleviates Muscle Atrophy and Restores Muscle Viability

Muscle viability is lost when nerve injury compromises neurological and electrical stimulation. Prolonged nerve denervation can lead to chronic muscle atrophy (Sun et al., 2017; Kollitz et al., 2018). Sciatic nerves manipulate gastrocnemius muscle, which in turn can reflect the neurological status. In addition, delayed muscle regeneration results in reduction in muscle contraction speed and force, along with a transformation from fast-twitch-type to slow-twitch-type muscle fiber (Zimowska et al., 2017). Therefore we measured gastrocnemius muscle weight and evaluated muscle morphology and muscle fiber type. At 6 and 12 weeks after surgery, the gastrocnemius muscle weight from COL/NC/PCL conduit was significantly higher than those from NC/PCL and PCL conduits ($p<0.05$), but it was significantly lower than that from the autograft ($p < 0.05$). There was no difference between the values of the COL/NC/PCL conduit and autograft at 18 weeks ($p > 0.05$, Figure S12). From the muscle fiber H&E and TB staining, a well-structured muscle fiber morphology was presented from the COL/NC/PCL conduit. The majority of area was filled with fast twitch phenotype fiber. In contrast, muscle samples from NC/PCL and PCL conduits displayed relatively irregular and

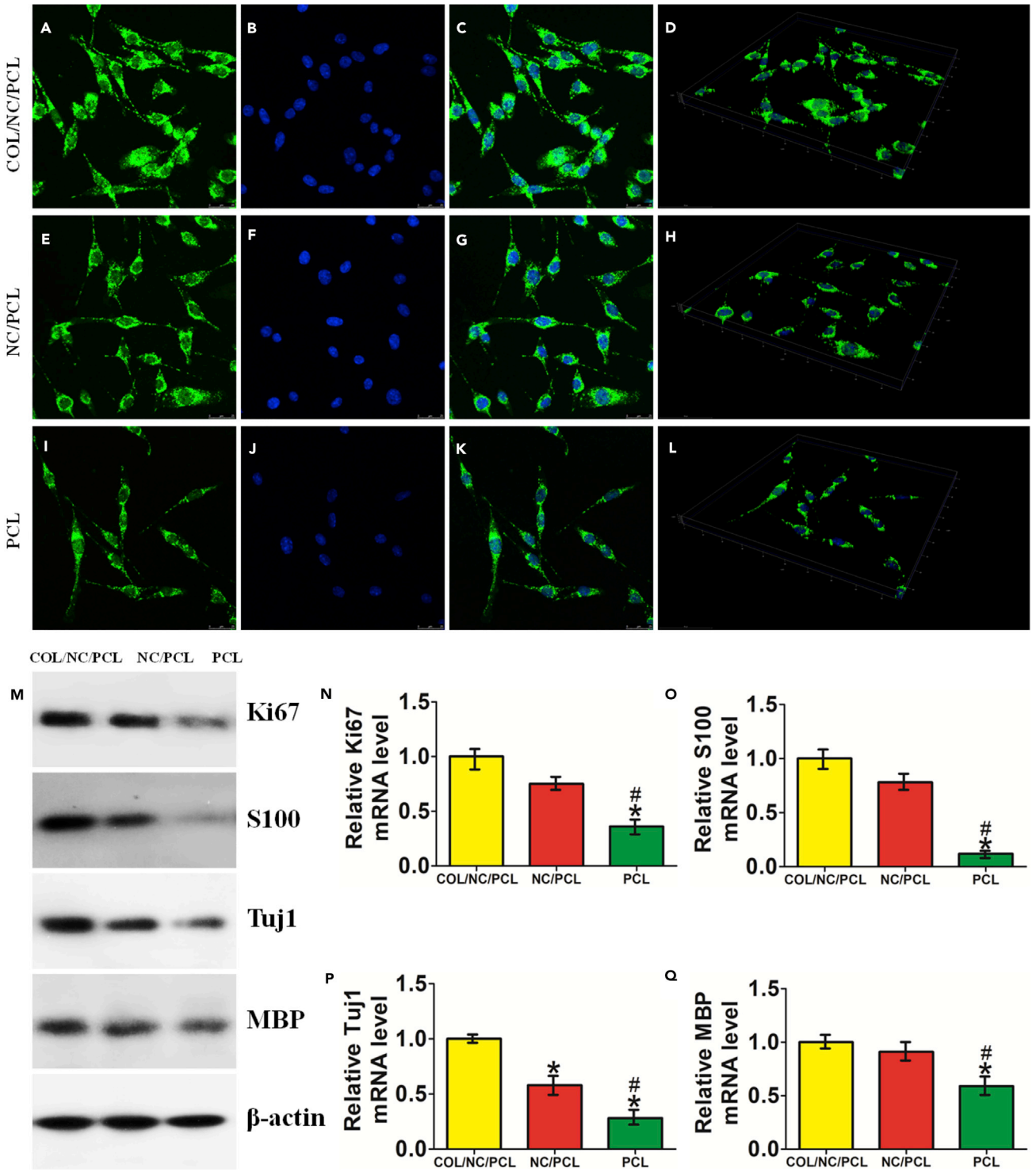

Figure 5. Immunofluorescence of MBP

(A–D) MBP expression in COL/NC/PCL.

(E–H) MBP expression in NC/PCL.

(I–L) MBP expression in PCL.

(A, E, and I) MBP staining; scale bars, 25 μm.

(B, F, and J) DAPI staining; scale bars, 25 μm.

(C, G, and K) Merged images; scale bars, 25 μm.

Figure 5. *Continued*
(D, H, and L) 3D display; scale bars, 50 μm.
(M) Western blots of Ki67, S100, Tuj1, and MBP compared among COL/NC/PCL, NC/PCL, and PCL conduits.
(N) Relative Ki67 mRNA level.
(O) Relative S100 mRNA level.
(P) Relative Tuj1 mRNA level.
(Q) Relative MBP mRNA level.
*$p < 0.05$ compared with COL/NC/PCL, $^{\#}p < 0.05$ compared with NC/PCL.

incomplete morphology. Most of the areas were occupied by slow-twitch-type muscle fiber. Laminin attaches the cytoskeleton structure to the ECM. Therefore it is an important protein in the process wherein skeletal muscle spreads forces and resists pressure in the surroundings (Holmberg and Durbeej, 2013). Better results were achieved from autograft and COL/NC/PCL conduit than the others (Figures S13–S18). It indicated that the COL/NC/PCL conduit evidently improved skeletal muscle restoration by ameliorating muscle atrophy.

COL/NC/PCL Inhibits Oxidative Stress and Inflammation in Long-Term Repair

Lasting oxidative stress and inflammatory reaction are harmful for effective axonal and myelin sheath regeneration. We evaluated the antioxidant and anti-inflammatory roles of nanoceria in long-range nerve defect for the first time, although nanoceria was confirmed to reduce ROS production and inflammatory adhesion previously (Oró et al., 2016). HO-1 can regulate redox homeostasis against ROS production and oxidant insult (Min et al., 2011). Its increased expression contributes to ROS clearance and cell protection (Xu et al., 2015). Nuclear factor-like 2 (Nrf2) is an upstream regulator of HO-1 family. Therefore, under oxidative environment, Nrf2 can activate HO-1 to strengthen antioxidative and anti-inflammatory reactions (Bao et al., 2016). We evaluated Nrf2 and HO-1 expression from different groups at three time points. Both COL/NC/PCL conduit and autograft showed the highest expression of both markers. NC/PCL conduit displayed more Nrf2 and HO-1 than PCL counterpart. In addition, we also included tumor necrosis factor α, Toll-like receptor 4, and IL-6. These markers are representatives for inflammatory status. Inflammation is the consequence of trauma-induced hypoxia in the nerve injury site. Macrophages gathered and released some pro-inflammatory molecules, leading to persistent tissue adhesion and compromised nerve regeneration (Lanza et al., 2012). We noticed that the inflammatory reaction was the most severe in PCL conduit, followed by NC/PCL counterpart. Nevertheless, COL/NC/PCL conduit and autograft only exhibited very mild inflammation, especially at 18 weeks after surgery (Figures S19–S22). It indicated that COL/NC/PCL conduit significantly reduced oxidative stress and inflammation after traumatic peripheral nerve damage.

Nanoceria Stimulates Ideal Angiogenesis in Nerve Tissue Surroundings

Angiogenesis is the process wherein new vessels form and provide nutrition to the surrounding tissues, like bones and nerves (Baker et al., 2011). Therefore, it is very vital to functional peripheral nerve regeneration. Nanoceria has a unique characteristic of inducing angiogenesis *in vivo*. This capability is also related to oxygen transfer and modulation in the intracellular environment (Das et al., 2012). Low ROS level is beneficial to angiogenesis. In contrast, high ROS level reduces angiogenic state. Nanoceria creates relatively low ROS microenvironment to stimulate ideal new vessel formation. In this study, we analyzed the angiogenic potential of nanoceria in long-range nerve defect *in vivo* for the first time. We included CD31 and CD34, two markers for angiogenesis (Luedi et al., 2018; Wang et al., 2017). The neovascularization was assessed upon several indicators, including microvessel density (MVD), vessel-like structure (VLS) area, and density ((VLS area+ CD31/CD34+ area)/total scaffold area) at 6, 12, and 18 weeks after surgery. The angiogenic status was very close between COL/NC/PCL and NC/PCL conduits, which was better than that of the PCL counterpart. However, autograft displayed the most prominent angiogenesis in all groups (Figures S23–S26). It was probably the higher vascular endothelial growth factor secretion from autologous nerves that contributed to better neovascularization in the surroundings (Hoben et al., 2015).

COL/NC/PCL Conduit Improves Axonal Regeneration, Remyelination, and Neural Viability

In addition to morphological evaluation of axonal and myelin regeneration, we also evaluated some markers, sox10, growth-associated protein-43 (GAP-43), S100, Tuj1, MBP, and neurofilament 200 (NF200). Sox10 promotes neurogenesis in peripheral nerve restoration after trauma (Dyachuk et al., 2014). GAP-43 is an important biomarker in the entire course of peripheral nerve regrowth (Kaneda

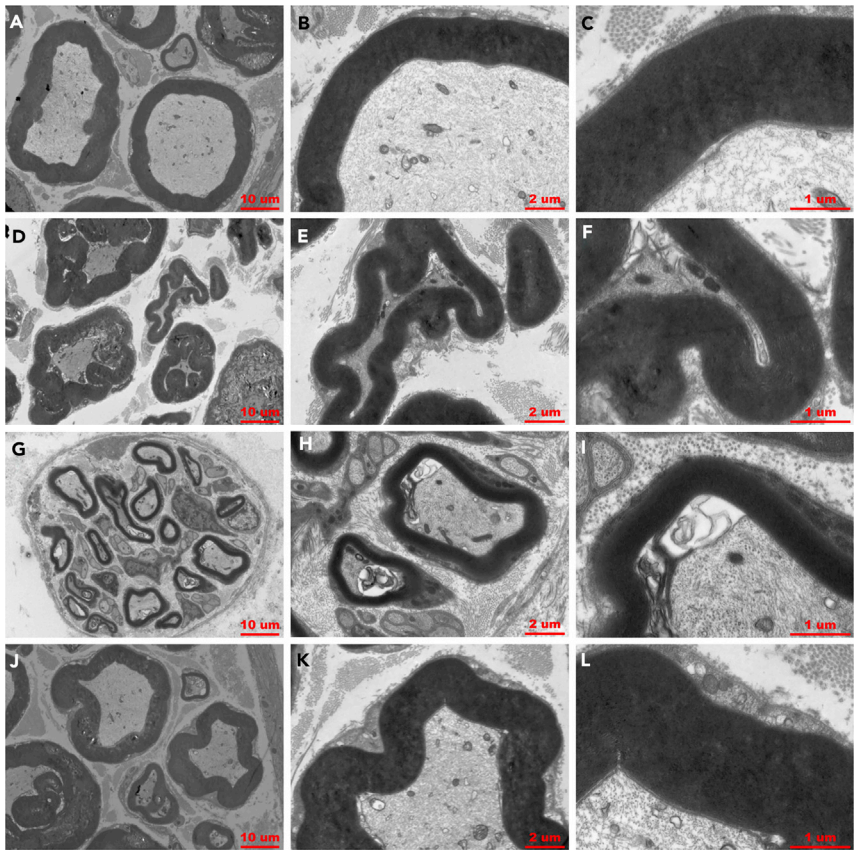

Figure 6. TEM for Axonal Regeneration and Remyelination State at 18 Weeks Postoperatively

(A–C) COL/NC/PCL conduit.

(D–F) NC/PCL conduit.

(G–I) PCL conduit.

(J–L) Autograft.

Scale bars, 10 μm in (A, D, G, and J); 2 μm in (B, E, H, and K); and 1 μm in (C, F, I, and L).

et al., 2010). S100, Tuj1, MBP, and NF200 are common markers involved in assessment of sciatic nerve recovery (Qian et al., 2018d). NF200 and Tuj1 can reflect axonal regeneration (Tian et al., 2017; Ansari et al., 2017). S100 indicates Schwann cell migration, and MBP represents neural fiber myelination (Uz et al., 2017; Feliú et al., 2017). At 6 and 12 weeks after surgery, sox10 and GAP-43 expression was higher in autograft than COL/NC/PCL conduit ($p<0.05$), and did not show significant differences between NC/PCL and PCL conduits ($p>0.05$). At 18 weeks, autograft and COL/NC/PCL conduit showed significantly higher sox10 and GAP-43 expression than the remaining groups ($p < 0.05$, Figures S27–S30). At 6 and 12 weeks after surgery, the autograft group showed better results in Tuj1, NF200, S100, and MBP expression than the remaining conduits ($p<0.05$). At 18 weeks, the expression of Tuj1, NF200, S100, and MBP was evidently up-regulated in COL/NC/PCL conduit. It was notoriously higher than those of the NC/PCL and PCL conduits ($p < 0.05$) and was slightly lower than those of the autograft at 6, 12 ($p>0.05$, Figures S31–S34), and 18 weeks ($p > 0.05$, Figures 7 and 8). It displayed that the COL/NC/PCL conduit significantly contributed to axonal regrowth and remyelination after severe long-range nerve defect.

Conclusions

In summary, we fabricated COL/NC/PCL nerve conduit via asymmetrical layer-by-layer 3D manufacture. The conduit was composed of three layers: the innermost NC/PCL mixed layer, the outermost COL layer, and the middle PCL layer. A microneedle on the tube assured even pore size, which allowed free exchanges of nutrients into the conduit. We evaluated the antioxidative stress and anti-inflammatory potential of COL/NC/PCL conduit both *in vitro* and *in vivo*. It evidently promoted better ROS clearance and inflammation inhibition. In addition, nanoceria-based conduit also contributed to

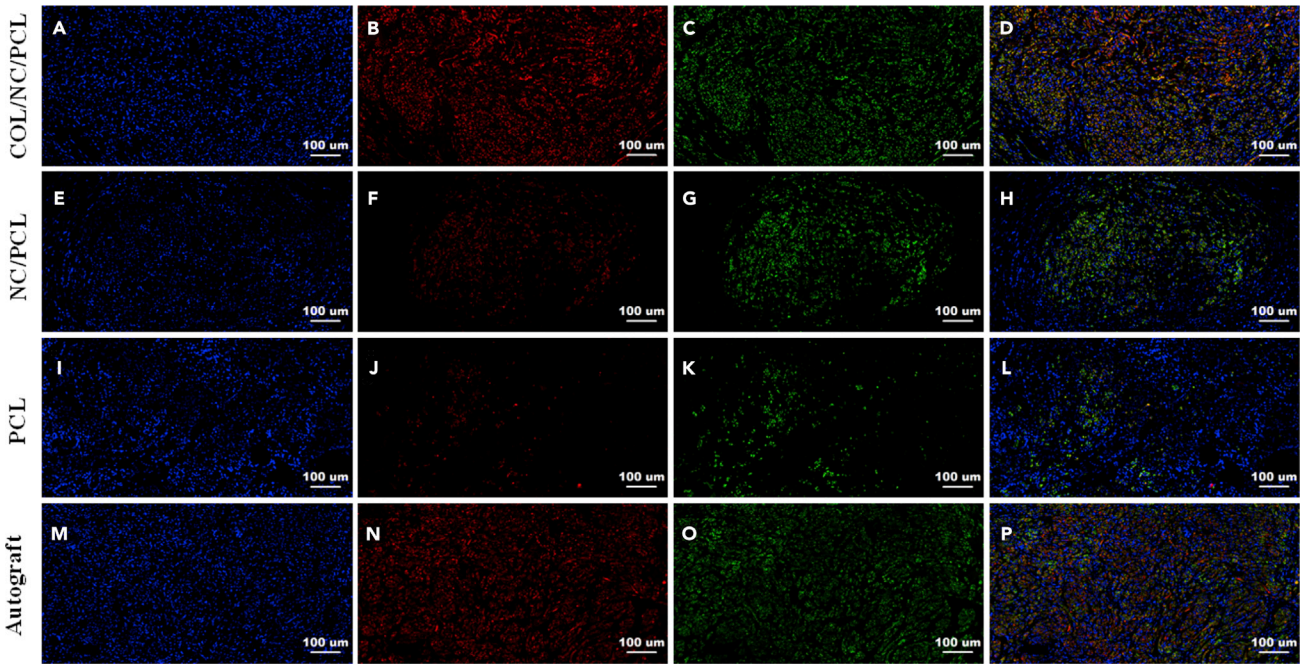

Figure 7. Triple Immunofluorescence of Regenerated Nerve Tissues Showing Axonal Restoration at 18 Weeks Postoperatively

(A–D) COL/NC/PCL.

(E–H) NC/PCL.

(I–L) PCL.

(M–P) Autograft.

(A, E, I, and M) DAPI staining.

(B, F, J, and N) NF200 staining.

(C, G, K, and O) Tuj1 staining.

(D, H, L, and P) Merged images.

Scale bars, 100 μm.

satisfactory axonal and myelin regeneration in severe sciatic nerve defect model at 18 weeks after surgery. This effect was further enhanced by collagen in the outermost layer via asymmetrical 3D manufacture because it assured fewer fibroblasts adhered either to the conduit or to the regenerated nerves. Moreover, we found that nanoceria stimulated angiogenesis after nerve injury, probably due to the proangiogenic microenvironment resulting from the low ROS production (Tojo et al., 2005). We believe our asymmetrical manufacture will provide more insights into the design of nerve conduit that combines suitable structural cues and controlled drug release. In addition, it paves a promising avenue to the integrated and fast fabrication of nerve scaffold. Nanoceria is characteristic of several important factors involved in nerve regeneration, such as oxygen modulation, angiogenic stimulation, and neural morphology reconstruction. Nanoceria-based biomaterials are considered to provide compelling evidence for future studies in antioxidant conduit and severe neurological defects in the nerve tissue engineering.

Limitations of the Study

In this study, we evaluated the asymmetrical fabrication of COL/NC/PCL composite channel for repairing large sciatic nerve defects. Although many advantages and functions were displayed, including its potential in improving tissue proliferation, adhesion, and antioxidant capacity, the possible mechanism behind these facts was not comprehensively investigated. In addition, we did not observe complete scaffold degradation at 18 weeks. It required further evaluation at longer time points *in vivo*.

METHODS

All methods can be found in the accompanying Transparent Methods supplemental file.

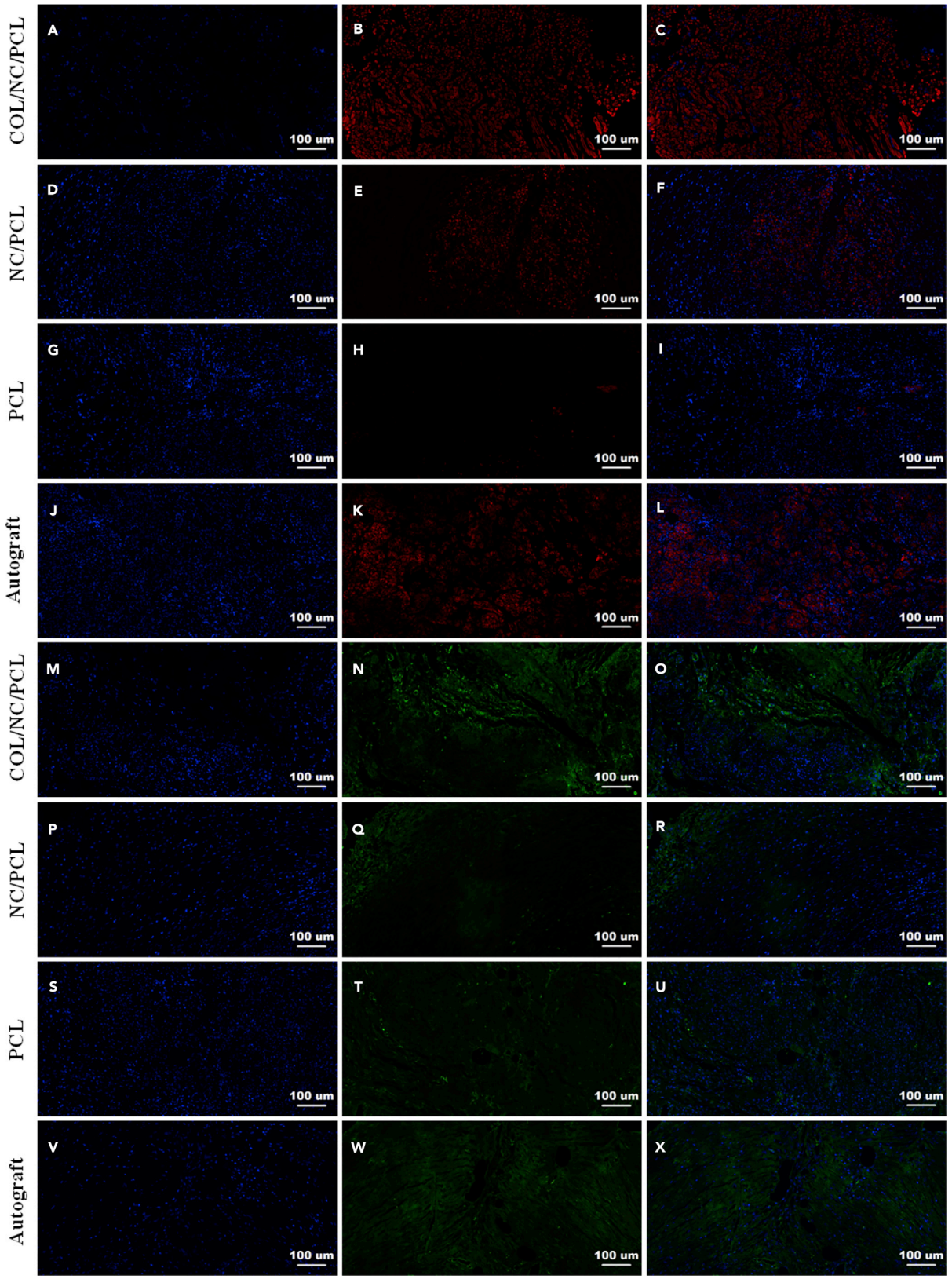
COL/NC/PCL
NC/PCL
PCL
Autograft
COL/NC/PCL
NC/PCL
PCL
Autograft
A
B
C
D
E
F
G
H
I
J
K
L
M
N
O
P
Q
R
S
T
U
V
W
X
100 um

Figure 8. Triple Immunofluorescence Showing Schwann Cell Viability and Remyelination at 18 Weeks Postoperatively

(A–X) (A–C and M–O) COL/NC/PCL. (D–F and P–R) NC/PCL. (G–I and S–U) PCL. (J–L and V–X) Autograft. (A, D, G, J, M, P, S, and V) DAPI staining. (B, E, H, and K) MBP staining. (N, Q, T, and W) S100 staining. (C, F, I, L, O, R, U, and X) Merged images.

Scale bars, 100 μm.

SUPPLEMENTAL INFORMATION

Supplemental Information includes Transparent Methods and 34 figures and can be found with this article online at https://doi.org/10.1016/j.isci.2019.01.013.

ACKNOWLEDGMENTS

The study was supported by the Projects of National Science Foundation of China (Grant Nos. 81830076, 81672146, 81570992 and 81571261), the Projects of National Science Foundation of Shanghai, China (Grant No. 17401901000), SUMHS Seed Foundation Project (Grant Nos. HMSF-16-21-010), Science and Technology Development Foundation of Pudong New District, Shanghai, China (Grant Nos. PKJ2016-Y55 and PWZxq2017-03), the Program of Shanghai Sixth People's Hospital East Campus Foundation (No.2019YY001), and The Program of Shanghai Sixth People's Hospital Foundation (No.LY2Y0272). The study was also partly sponsored by the Interdisciplinary Program of Shanghai Jiao Tong University (Nos. ZH2018QNA56 and YG2017MS22). We appreciate the help from the faculty of the Instrumental Analysis Center (IAC) of Shanghai Jiao Tong University.

AUTHOR CONTRIBUTIONS

W.E.Y. conceived the initial idea and the conceptualization. C.F. and W.E.Y. designed the study, participated in data extraction and analysis, and revised the manuscript. Y.Q., X.Z., Q.H., H.L., W.E.Y., and C.F. participated in the study design, searched databases, extracted and assessed studies, and helped draft the manuscript. Y.Q. wrote the manuscript. All authors have read and approved the final manuscript.

DECLARATION OF INTERESTS

The authors declare no competing interests.

Received: July 4, 2018
Revised: December 24, 2018
Accepted: January 8, 2019
Published: February 22, 2019

REFERENCES

Ansari, S., Diniz, I.M., Chen, C., Sarrion, P., Tamayol, A., Wu, B.M., and Moshaverinia, A. (2017). Human periodontal ligament- and gingiva-derived mesenchymal stem cells promote nerve regeneration when encapsulated in alginate/hyaluronic acid 3D scaffold. Adv. Healthc. Mater. *6*, https://doi.org/10.1002/adhm.201700670.

Arya, A., Gangwar, A., Singh, S.K., Roy, M., Das, M., Sethy, N.K., and Bhargava, K. (2016). Cerium oxide nanoparticles promote neurogenesis and abrogate hypoxia-induced memory impairment through AMPK-PKC-CBP signaling cascade. Int. J. Nanomed. *11*, 1159–1173.

Baker, M., Robinson, S.D., Lechertier, T., Barber, P.R., Tavora, B., D'Amico, G., Jones, D.T., Vojnovic, B., and Hodivala-Dilke, K. (2011). Use of the mouse aortic ring assay to study angiogenesis. Nat. Protoc. *7*, 89–104.

Bao, J., Ding, R., Zou, L., Zhang, C., Wang, K., Liu, F., Li, P., Chen, M., Wan, J.B., Su, H., et al. (2016). Forsythiae fructus inhibits B16 melanoma growth involving MAPKs/Nrf2/HO-1 mediated anti-oxidation and anti-inflammation. Am. J. Chin. Med. *44*, 1043–1061.

Carrier-Ruiz, A., Evaristo-Mendonça, F., Mendez-Otero, R., and Ribeiro-Resende, V.T. (2015). Biological behavior of mesenchymal stem cells on poly-ε-caprolactone filaments and a strategy for tissue engineering of segments of the peripheral nerves. Stem Cell Res. Ther. *6*, 128.

Ciofani, G., Genchi, G.G., Liakos, I., Cappello, V., Gemmi, M., Athanassiou, A., Mazzolai, B., and Mattoli, V. (2013). Effects of cerium oxide nanoparticles on PC12 neuronal-like cells: proliferation, differentiation, and dopamine secretion. Pharm. Res. *30*, 2133–2145.

D'Angelo, B., Santucci, S., Benedetti, E., Di Loreto, S., Phani, R., Falone, S., Amicarelli, F., Ceru, M., and Cimini, A. (2009). Cerium oxide nanoparticles trigger neuronal survival in a human Alzheimer disease model by modulating BDNF pathway. Curr. Nanosci. *5*, 167–176.

Das, S., Singh, S., Dowding, J.M., Oommen, S., Kumar, A., Sayle, T.X., Saraf, S., Patra, C.R., Vlahakis, N.E., Sayle, D.C., et al. (2012). The induction of angiogenesis by cerium oxide nanoparticles through the modulation of oxygen in intracellular environments. Biomaterials *33*, 7746–7755.

DeCoteau, W., Heckman, K.L., Estevez, A.Y., Reed, K.J., Costanzo, W., Sandford, D., Studlack, P., Clauss, J., Nichols, E., Lipps, J., et al. (2016). Cerium oxide nanoparticles with antioxidant properties ameliorate strength and prolong life in mouse model of amyotrophic lateral sclerosis. Nanomedicine *12*, 2311–2320.

Dyachuk, V., Furlan, A., Shahidi, M.K., Giovenco, M., Kaukua, N., Konstantinidou, C., Pachnis, V., Memic, F., Marklund, U., Müller, T., et al. (2014). Parasympathetic neurons originate from nerve-associated peripheral glial progenitors. Science *345*, 82–87.

Estevez, A.Y., Pritchard, S., Harper, K., Aston, J.W., Lynch, A., Lucky, J.J., Ludington, J.S., Chatani, P., Mosenthal, W.P., Leiter, J.C., et al.

(2011). Neuroprotective mechanisms of cerium oxide nanoparticles in a mouse hippocampal brain slice model of ischemia. Free Radic. Biol. Med. *51*, 1155–1163.

Feliú, A., Bonilla Del Río, I., Carrillo-Salinas, F.J., Hernández-Torres, G., Mestre, L., Puente, N., Ortega-Gutiérrez, S., López-Rodríguez, M.L., Grandes, P., Mecha, M., et al. (2017). 2-arachidonoylglycerol reduces proteoglycans and enhances remyelination in a progressive model of demyelination. J. Neurosci. *37*, 8385–8398.

Gliga, A.R., Edoff, K., Caputo, F., Källman, T., Blom, H., Karlsson, H.L., Ghibelli, L., Traversa, E., Ceccatelli, S., and Fadeel, B. (2017). Cerium oxide nanoparticles inhibit differentiation of neural stem cells. Sci. Rep. *7*, 9284.

Guan, Y., Li, M., Dong, K., Gao, N., Ren, J., Zheng, Y., and Qu, X. (2016). Ceria/POMs hybrid nanoparticles as a mimicking metallopeptidase for treatment of neurotoxicity of amyloid-β peptide. Biomaterials *98*, 92–102.

Hoben, G., Yan, Y., Iyer, N., Newton, P., Hunter, D.A., Moore, A.M., Sakiyama-Elbert, S.E., Wood, M.D., and Mackinnon, S.E. (2015). Comparison of acellular nerve allograft modification with Schwann cells or VEGF. Hand *10*, 396–402.

Holmberg, J., and Durbeej, M. (2013). Laminin-211 in skeletal muscle function. Cell Adh. Migr. *7*, 111–121.

Ishikawa, Y., Takeda, M., Tsukimoto, S., Nakayama, K.S., and Asao, N. (2016). Cerium oxide nanorods with unprecedented low-temperature oxygen storage capacity. Adv. Mater. *28*, 1467–1471.

Jia, J., Zhang, T., Chi, J., Liu, X., Sun, J., Xie, Q., Peng, S., Li, C., and Yi, L. (2018). Neuroprotective effect of CeO2@PAA-LXW7 against H2O2-induced cytotoxicity in NGF-differentiated PC12 cells. Neurochem. Res. https://doi.org/10.1007/s11064-018-2559-y.

Kaneda, M., Nagashima, M., Mawatari, K., Nunome, T., Muramoto, K., Sugitani, K., and Kato, S. (2010). Growth-associated protein43 (GAP43) is a biochemical marker for the whole period of fish optic nerve regeneration. Adv. Exp. Med. Biol. *664*, 97–104.

Khaksar, M.R., Rahimifard, M., Baeeri, M., Maqbool, F., Navaei-Nigjeh, M., Hassani, S., Moeini-Nodeh, S., Kebriaeezadeh, A., and Abdollahi, M. (2017). Protective effects of cerium oxide and yttrium oxide nanoparticles on reduction of oxidative stress induced by sub-acute exposure to diazinon in the rat pancreas. J. Trace Elem. Med. Biol. *41*, 79–90.

Kerasnoudis, A., Pitarokoili, K., Behrendt, V., Gold, R., and Yoon, M.S. (2014). Multifocal motor neuropathy: correlation of nerve ultrasound, electrophysiological, and clinical findings. Peripher. Nerv. Syst. *19*, 165–174.

Kollitz, K.M., Giusti, G., Friedrich, P.F., Bishop, A.T., and Shin, A.Y. (2018). Validation of isometric tetanic force as a measure of muscle recovery after nerve injury in the rabbit biceps. J. Hand Surg. Am. *43*, 488.e1–488.e8.

Kuroyanagi, M., Yamamoto, A., Shimizu, N., Toi, A., Inomata, T., Takeda, A., and Kuroyanagi, Y. (2014). Development of anti-adhesive spongy sheet composed of hyaluronic acid and collagen containing epidermal growth factor. J. Biomater. Sci. Polym. Ed. *25*, 1253–1265.

Lanza, C., Raimondo, S., Vergani, L., Catena, N., Sénès, F., Tos, P., and Geuna, S. (2012). Expression of antioxidant molecules after peripheral nerve injury and regeneration. J. Neurosci. Res. *90*, 842–848.

Luedi, M.M., Singh, S.K., Mosley, J.C., Hassan, I.S.A., Hatami, M., Gumin, J., Andereggen, L., Sulman, E.P., Lang, F.F., Stueber, F., et al. (2018). Dexamethasone-mediated oncogenicity in vitro and in an animal model of glioblastoma. J. Neurosurg. *12*, 1–10.

Marino, A., Ciofani, G., Filippeschi, C., Pellegrino, M., Pellegrini, M., Orsini, P., Pasqualetti, M., Mattoli, V., and Mazzolai, B. (2013). Two-photon polymerization of sub-micrometric patterned surfaces: investigation of cell-substrate interactions and improved differentiation of neuron-like cells. ACS Appl. Mater. Interfaces *5*, 13012–13021.

Marino, A., Tonda-Turo, C., De Pasquale, D., Ruini, F., Genchi, G., Nitti, S., Cappello, V., Gemmi, M., Mattoli, V., Ciardelli, G., et al. (2017). Gelatin/nanoceria nanocomposite fibers as antioxidant scaffolds for neuronal regeneration. Biochim. Biophys. Acta *1861*, 386–395.

Min, K.J., Lee, J.T., Joe, E.H., and Kwon, T.K. (2011). An IκBα phosphorylation inhibitor induces heme oxygenase-1(HO-1) expression through the activation of reactive oxygen species (ROS)-Nrf2-ARE signaling and ROS-PI3K/Akt signaling in an NF-κB-independent mechanism. Cell Signal. *23*, 1505–1513.

Mitra, R.N., Gao, R., Zheng, M., Wu, M.J., Voinov, M.A., Smirnov, A.I., Smirnova, T.I., Wang, K., Chavala, S., and Han, Z. (2017). Glycol chitosan engineered autoregenerative antioxidant significantly attenuates pathological damages in models of age-related macular degeneration. ACS Nano *11*, 4669–4685.

Najafi, R., Hosseini, A., Ghaznavi, H., Mehrzadi, S., and Sharifi, A.M. (2017). Neuroprotective effect of cerium oxide nanoparticles in a rat model of experimental diabetic neuropathy. Brain Res. Bull. *131*, 117–122.

Oró, D., Yudina, T., Fernández-Varo, G., Casals, E., Reichenbach, V., Casals, G., González de la Presa, B., Sandalinas, S., Carvajal, S., Puntes, V., et al. (2016). Cerium oxide nanoparticles reduce steatosis, portal hypertension and display anti-inflammatory properties in rats with liver fibrosis. J. Hepatol. *64*, 691–698.

Pagliari, F., Mandoli, C., Forte, G., Magnani, E., Pagliari, S., Nardone, G., Licoccia, S., Minieri, M., Di Nardo, P., and Traversa, E. (2012). Cerium oxide nanoparticles protect cardiac progenitor cells from oxidative stress. ACS Nano *6*, 3767–3775.

Qian, Y., Han, Q., Zhao, X., Song, J., Cheng, Y., Fang, Z., Ouyang, Y., Yuan, W.E., and Fan, C. (2018a). 3D melatonin nerve scaffold reduces oxidative stress and inflammation and increases autophagy in peripheral nerve regeneration. J. Pineal Res. *65*, e12516.

Qian, Y., Song, J., Zhao, X., Chen, W., Ouyang, Y., Yuan, W., and Fan, C. (2018b). 3D fabrication with integration molding of a graphene oxide/polycaprolactone nanoscaffold for neurite regeneration and angiogenesis. Adv. Sci. *5*, 1700499.

Qian, Y., Song, J., Zheng, W., Zhao, X., Ouyang, Y., Yuan, W., and Fan, C. (2018c). 3D manufacture of gold nanocomposite channels facilitates neural differentiation and regeneration. Adv. Funct. Mater. *28*, 1707077.

Qian, Y., Zhao, X., Han, Q., Chen, W., Li, H., and Yuan, W. (2018d). An integrated multi-layer 3D-fabrication of PDA/RGD coated graphene loaded PCL nanoscaffold for peripheral nerve restoration. Nat. Commun. *9*, 323.

Qiu, T., Yin, Y., Li, B., Xie, L., Yan, Q., Dai, H., Wang, X., and Li, S. (2014). PDLLA/PRGD/β-TCP conduits build the neurotrophin-rich microenvironment suppressing the oxidative stress and promoting the sciatic nerve regeneration. J. Biomed. Mater.Res. A *102*, 3734–3743.

Rasekh, M., Ahmad, Z., Frangos, C.C., Bozec, L., Edirisinghe, M., and Day, R.M. (2013). Spatial and temporal evaluation of cell attachment to printed polycaprolactone microfibres. Acta Biomater. *9*, 5052–5062.

Sharifi, F., Patel, B.B., Dzuilko, A.K., Montazami, R., Sakaguchi, D.S., and Hashemi, N. (2016). Polycaprolactone microfibrous scaffolds to navigate neural stem cells. Biomacromolecules *17*, 3287–3297.

Sun, Y., Jin, C., Li, K., Zhang, Q., Geng, L., Liu, X., and Zhang, Y. (2017). Restoration of orbicularis oculi muscle function in rabbits with peripheral facial paralysis via an implantable artificial facial nerve system. Exp. Ther. Med. *14*, 5289–5296.

Tang, S., Yang, W., and Mao, X. (2007). Agarose/collagen composite scaffold as an anti-adhesive sheet. Biomed. Mater. *2*, S129–S134.

Tian, T., Yu, Z., Zhang, N., Chang, Y., Zhang, Y., Zhang, L., Zhou, S., Zhang, C., Feng, G., and Huang, F. (2017). Modified acellular nerve-delivering PMSCs improve functional recovery in rats after complete spinal cord transection. Biomater.Sci. *5*, 2480–2492.

Tojo, T., Ushio-Fukai, M., Yamaoka-Tojo, M., Ikeda, S., Patrushev, N., and Alexander, R.W. (2005). Role of gp91phox (Nox2)-containing NAD(P)H oxidase in angiogenesis in response to hindlimb ischemia. Circulation *111*, 2347–2355.

Uz, M., Büyüköz, M., Sharma, A.D., Sakaguchi, D.S., Altinkaya, S.A., and Mallapragada, S.K. (2017). Gelatin-based 3D conduits for transdifferentiation of mesenchymal stem cells into Schwann cell-like phenotypes. Acta Biomater. *53*, 293–306.

Vassie, J.A., Whitelock, J.M., and Lord, M.S. (2017). Endocytosis of cerium oxide nanoparticles and modulation of reactive oxygen species in human ovarian and colon cancer cells. Acta Biomater. *50*, 127–141.

Wang, H., Zhu, H., Guo, Q., Qian, T., Zhang, P., Li, S., Xue, C., and Gu, X. (2017). Overlapping mechanisms of peripheral nerve regeneration

and angiogenesis following sciatic nerve transection. Front. Cell. Neurosci. *11*, 323.

Xu, X., Li, H., Hou, X., Li, D., He, S., Wan, C., Yin, P., Liu, M., Liu, F., and Xu, J. (2015). Punicalagin induces Nrf2/HO-1 expression via upregulation of PI3K/AKT pathway and inhibits LPS-induced oxidative stress in RAW264.7 macrophages. Mediators Inflamm. *2015*, 380218.

Yao, C., Wang, W., Wang, P., Zhao, M., Li, X., and Zhang, F. (2018). Near-infrared upconversion mesoporous cerium oxide hollow biophotocatalyst for concurrent pH-/H_2O_2-responsive O_2-evolving synergetic cancer therapy. Adv. Mater. *30*, https://doi.org/10.1002/adma.201704833.

Yarar, E., Kuruoglu, E., Kocabıcak, E., Altun, A., Genc, E., Ozyurek, H., Kefeli, M., Marangoz, A.H., Aydın, K., and Cokluk, C. (2015). Electrophysiological and histopathological effects of mesenchymal stem cells in treatment of experimental rat model of sciatic nerve injury. Int. J. Clin. Exp. Med. *8*, 8776–8784.

Yi, J., Jiang, N., Li, B., Yan, Q., Qiu, T., Swaminatha Iyer, K., Yin, Y., Dai, H., Yetisen, A.K., and Li, S. (2018). Painful terminal neuroma prevention by capping PRGD/PDLLA conduit in rat sciatic nerves. Adv. Sci. *5*, 1700876.

Zimowska, M., Kasprzycka, P., Bocian, K., Delaney, K., Jung, P., Kuchcinska, K., Kaczmarska, K., Gladysz, D., Streminska, W., and Ciemerych, M.A. (2017). Inflammatory response during slow- and fast-twitch muscle regeneration. Muscle Nerve *55*, 400–409.

ISCI, Volume *12*

Supplemental Information

Asymmetrical 3D Nanoceria Channel for Severe Neurological Defect Regeneration

Yun Qian, Qixin Han, Xiaotian Zhao, Hui Li, Wei-En Yuan, and Cunyi Fan

Supporting Information

Figure legends

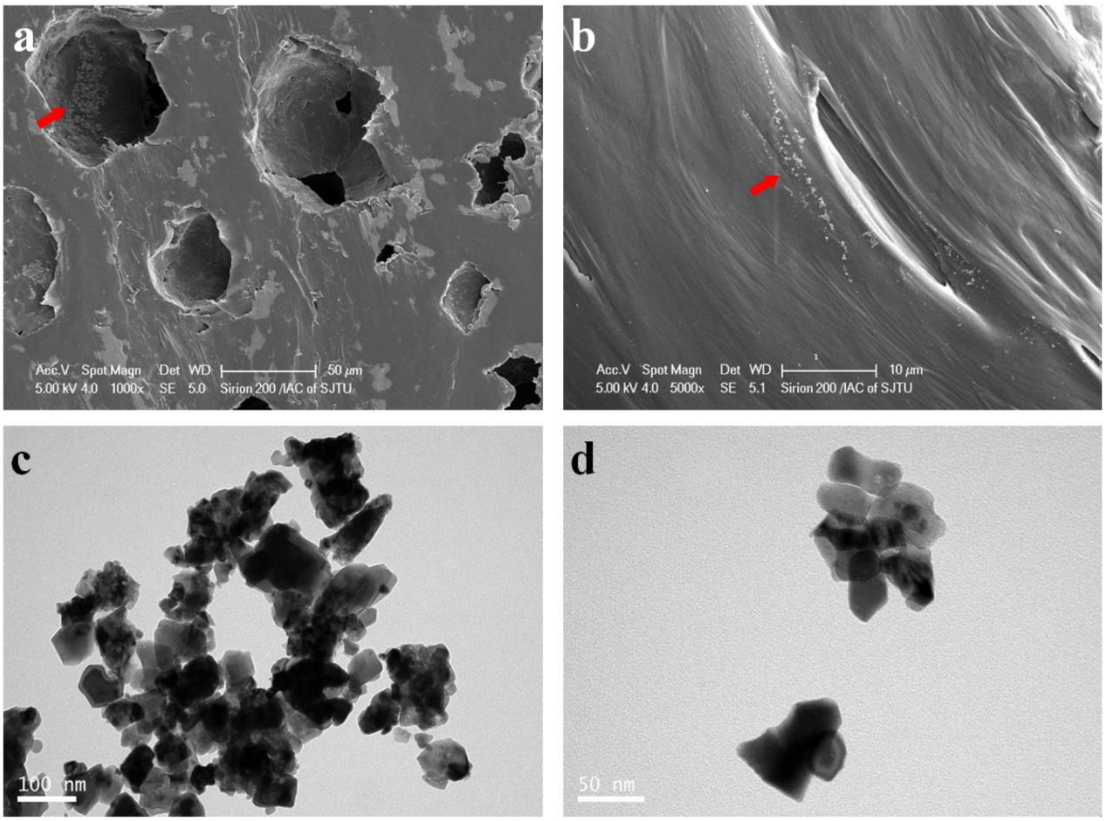

Figure S1. Nanoceria distribution in the cross section of scaffolds using scanning electron microscopy (SEM). a) scale bar=50μm, b) scale bar=10μm. Nanoceria were marked by red arrows. Nanoceria morphology evaluation using transmission electron microscopy (TEM). c) scale bar=100nm, d) scale bar=50nm , related to Figure 1.

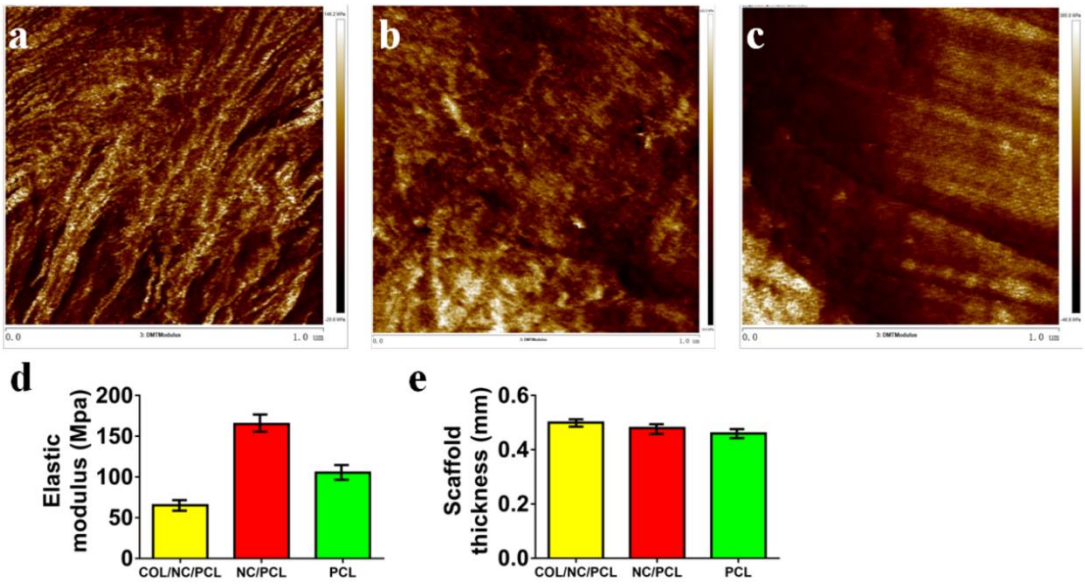

Figure S2. Mechanical properties of the scaffolds. Atomic force microscopy (AFM) for a) COL/NC/PCL, b) NC/PCL and c) PCL conduits. d) Elastic modulus of COL/NC/PCL, NC/PCL and PCL conduits. e) Scaffold thickness of COL/NC/PCL, NC/PCL and PCL conduits, related to Figure 1.

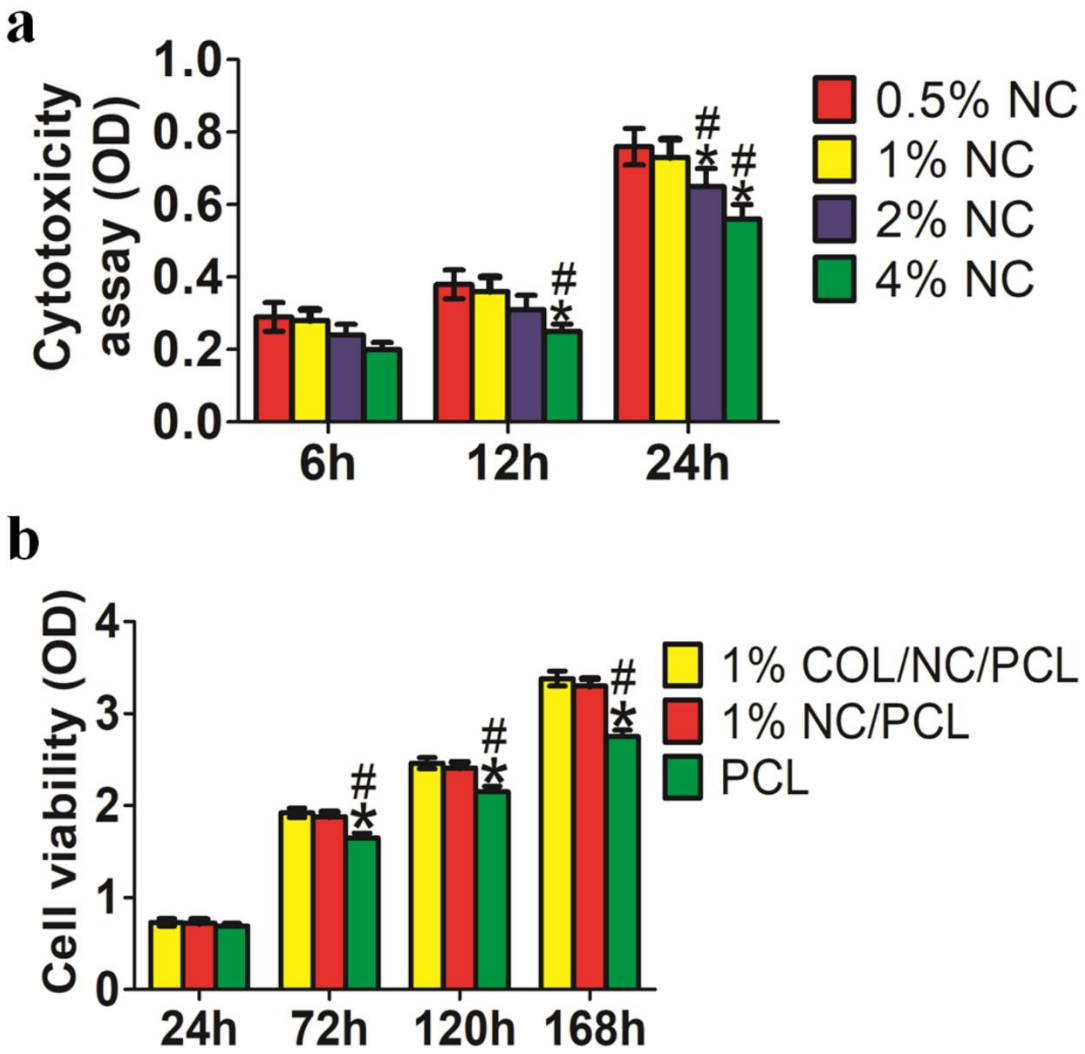

Figure S3. **Cell viability analysis by CCK8 assay.** a) Cytotoxicity assay (OD) examined at 6, 12 and 24h, $^{*}p<0.05$ compared with 0.5% NC, $^{\#}p<0.05$ compared with 1% NC. b) Cell viability (OD) examined at 24, 72, 120 and 168h, $^{*}p<0.05$ compared with 1% COL/NC/PCL, $^{\#}p<0.05$ compared with 1% NC/PCL, related to Figure 2.

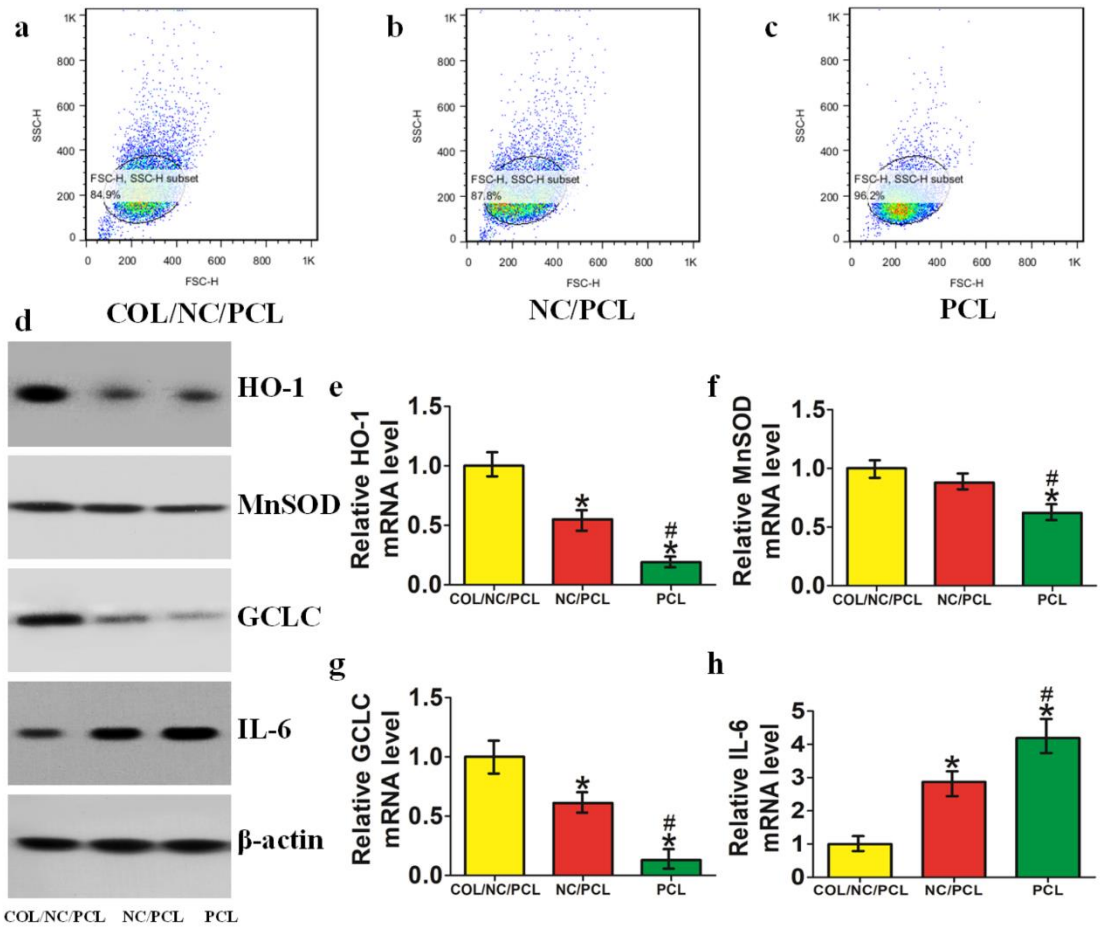

Figure S4. **Oxidative stress and inflammation evaluation.** Flow cytometry assay showing oxidative stress level compared among a) COL/NC/PCL. b) NC/PCL. c) PCL. d) Western blots of HO-1, MnSOD, GCLC and IL-6 compared among COL/NC/PCL, NC/PCL and PCL conduits. e) Relative HO-1 mRNA level. f) Relative MnSOD mRNA level. g) Relative GCLC mRNA level. h) Relative IL-6 mRNA level. $^{*}p<0.05$ compared with COL/NC/PCL, $^{\#}p<0.05$ compared with NC/PCL, related to Figure 3,4,5.

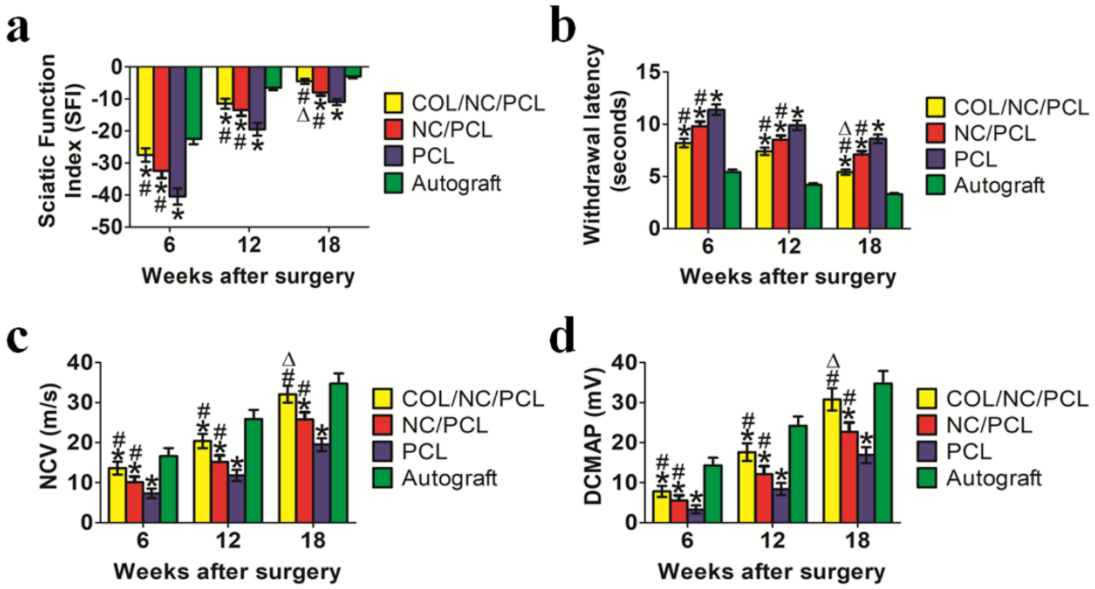

Figure S5. **Functional and electrophysiological evaluation of nerve regeneration at 6, 12 and 18 weeks after surgery.** a) Sciatic Function Index (SFI). b) Withdrawal latency (seconds). c) NCV (m/s). d) DCMAP (mV). $^{*}p<0.05$ compared with autograft, $^{\#}p<0.05$ compared with PCL, $^{\Delta}p<0.05$ compared with NC/PCL, related to Figure 6.

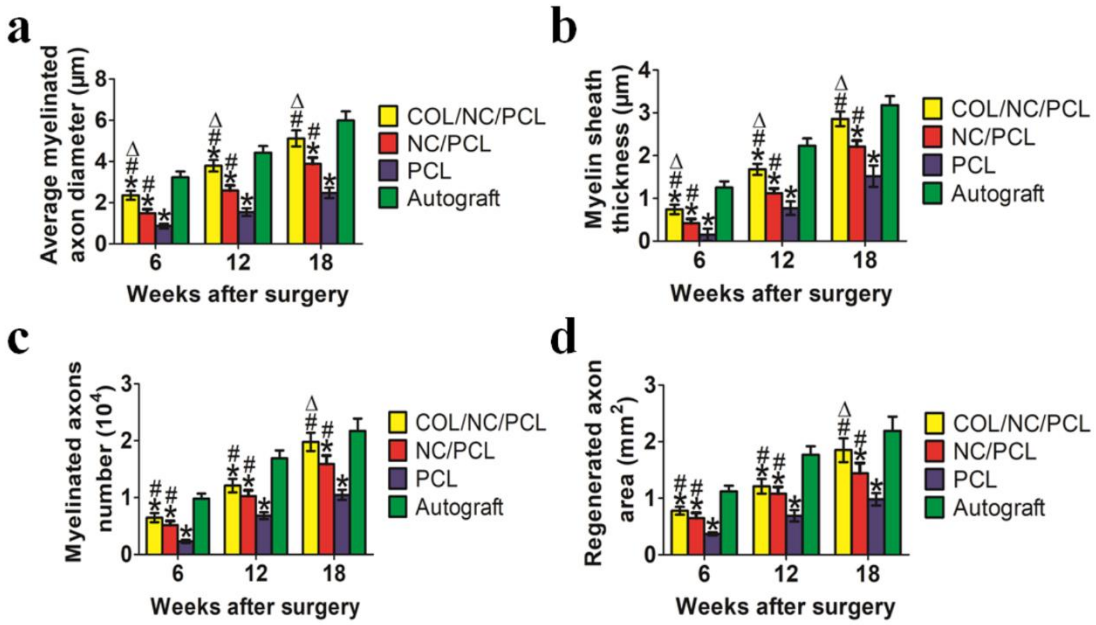

Figure S6. **Morphological evaluation of nerve regeneration at 6, 12 and 18 weeks after surgery.** a) Average myelinated axon diameter (μm). b) Myelin sheath thickness (μm). c) Myelinated axons number (10^4). d) Regenerated axon area (mm^2). $^{*}p<0.05$ compared with autograft, $^{\#}p<0.05$ compared with PCL, $^{\Delta}p<0.05$ compared with NC/PCL, related to Figure 6.

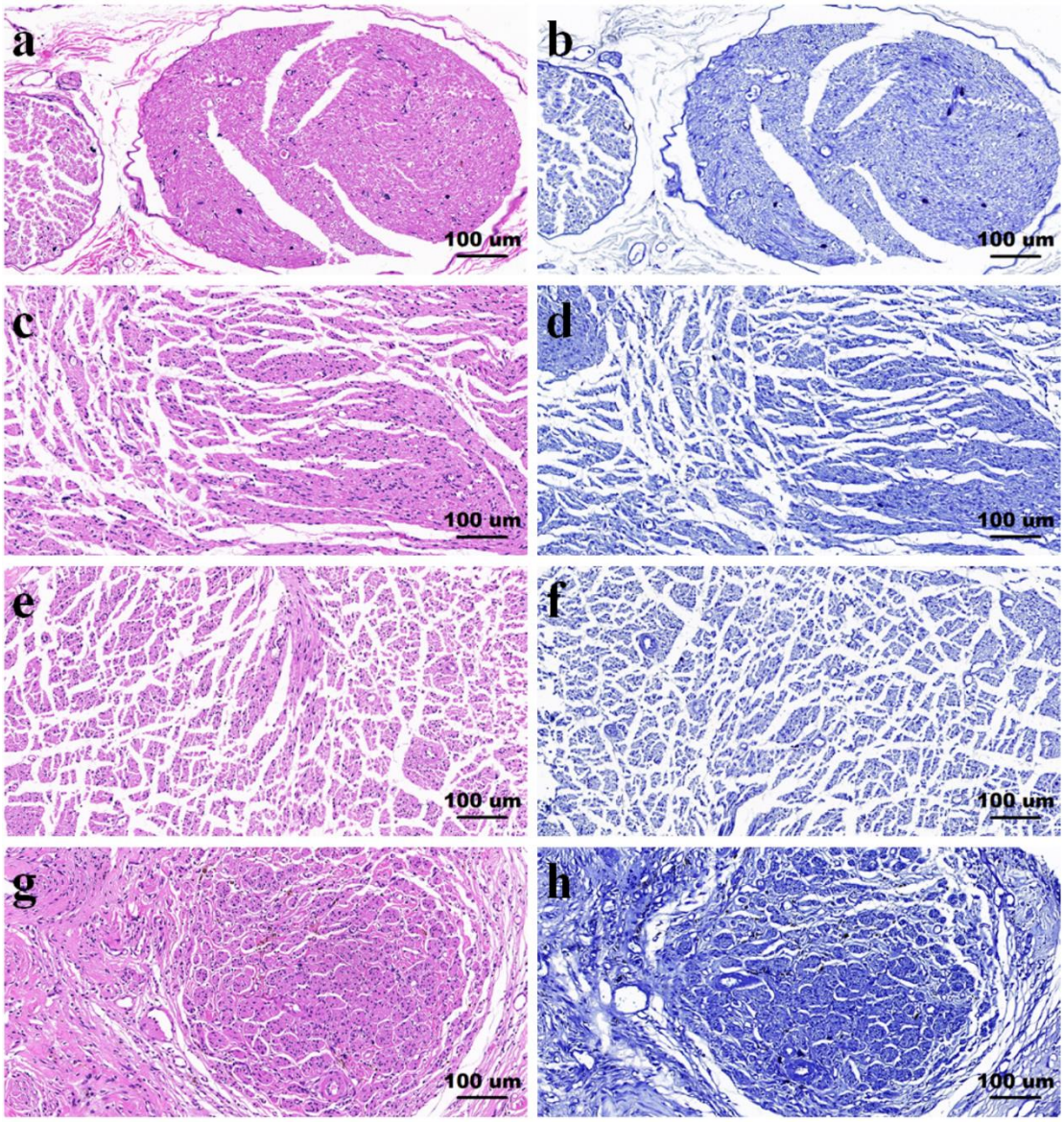

Figure S7. **HE (a, c, e, g) and TB (b, d, f, h) staining showing regenerated nerve morphology at 6 weeks postoperatively.** a, b) COL/NC/PCL. c, d) NC/PCL. e, f) PCL. g, h) Autograft. Scale bar = 100 μm, related to Figure 6.

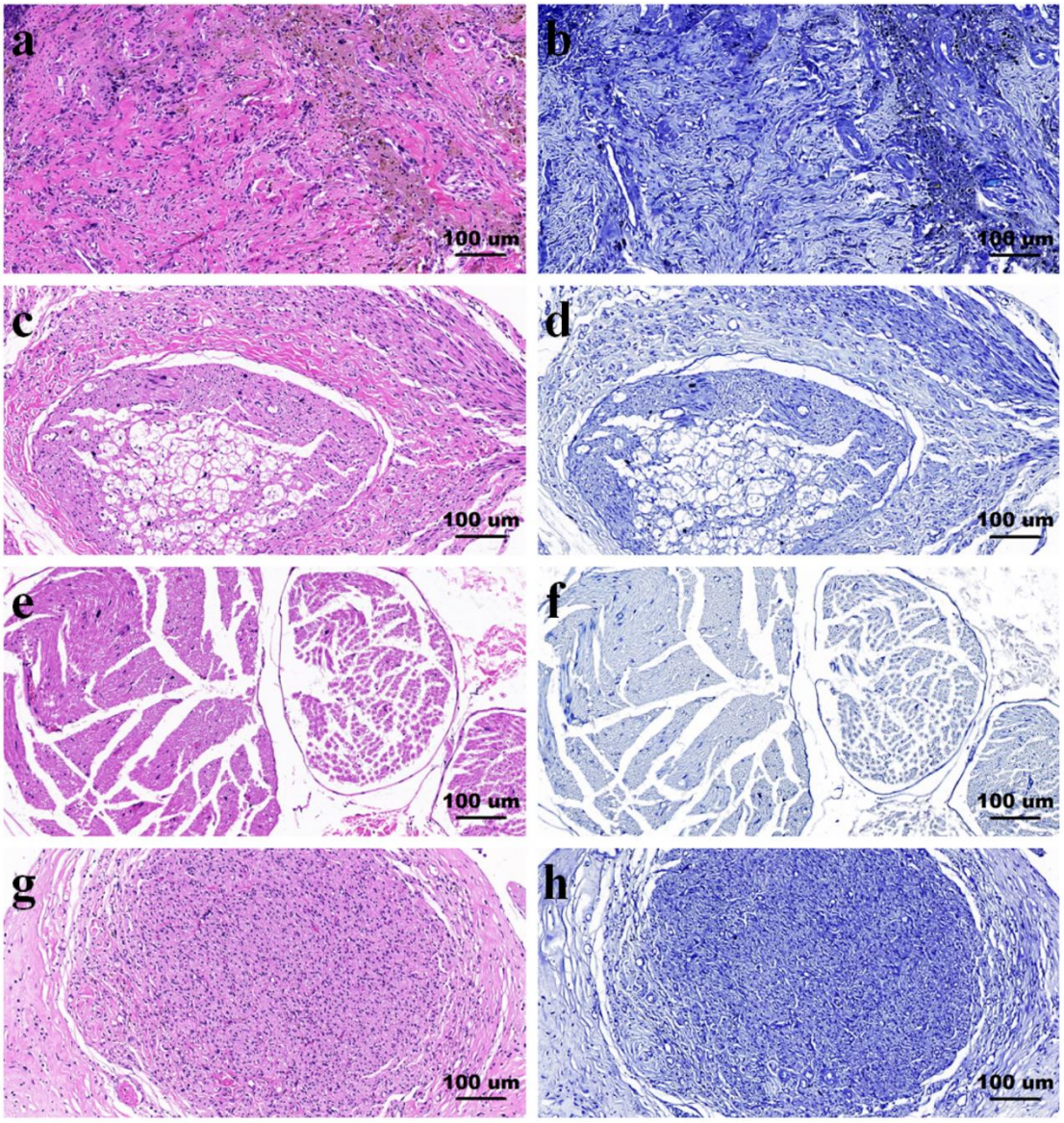

Figure S8. **HE (a, c, e, g) and TB (b, d, f, h) staining showing regenerated nerve morphology at 12 weeks postoperatively.** a, b) COL/NC/PCL. c, d) NC/PCL. e, f) PCL. g, h) Autograft. Scale bar = 100 μm, related to Figure 6.

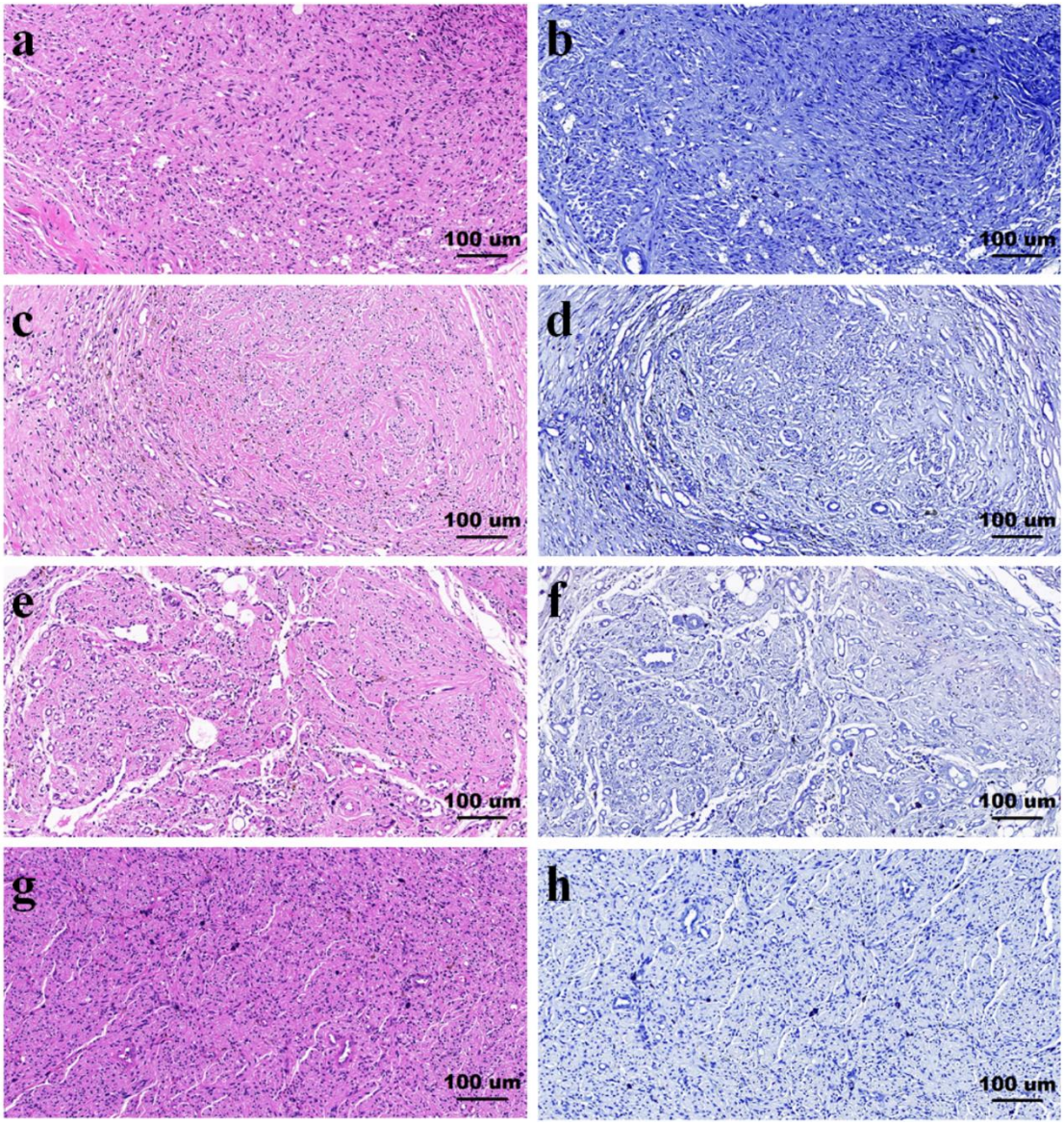

Figure S9. **HE (a, c, e, g) and TB (b, d, f, h) staining showing regenerated nerve morphology at 18 weeks postoperatively.** a, b) COL/NC/PCL. c, d) NC/PCL. e, f) PCL. g, h) Autograft. Scale bar = 100 μm, related to Figure 6.

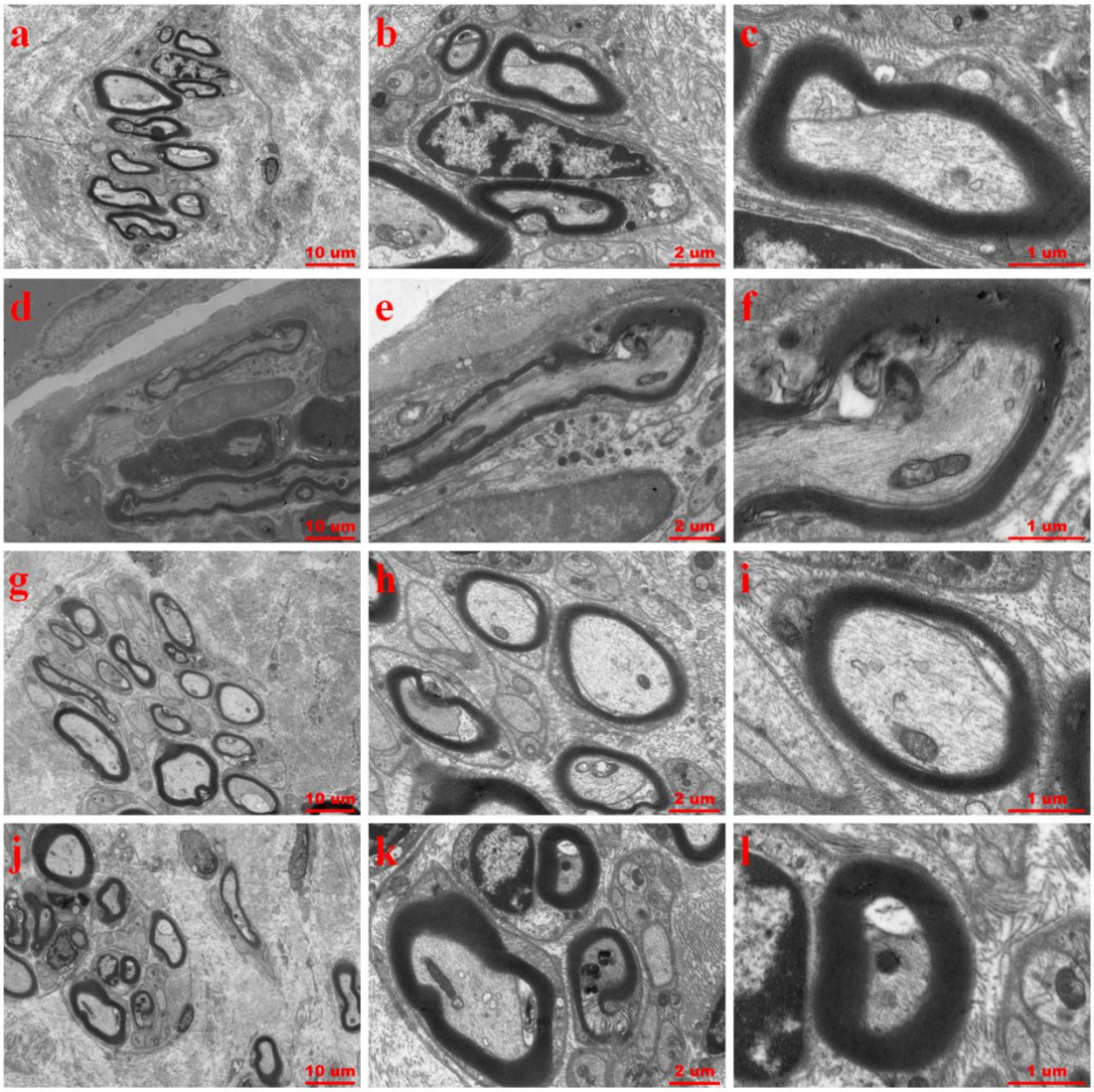

Figure S10. **TEM for axonal regeneration and remyelination state at 6 weeks postoperatively.** a-c) COL/NC/PCL. d-f) NC/PCL. g-i) PCL. j-l) Autograft. Scale bar = 10 μm in a, d, g, j). Scale bar = 2 μm in b, e, h, k). Scale bar = 1 μm in c, f, i, l), related to Figure 6.

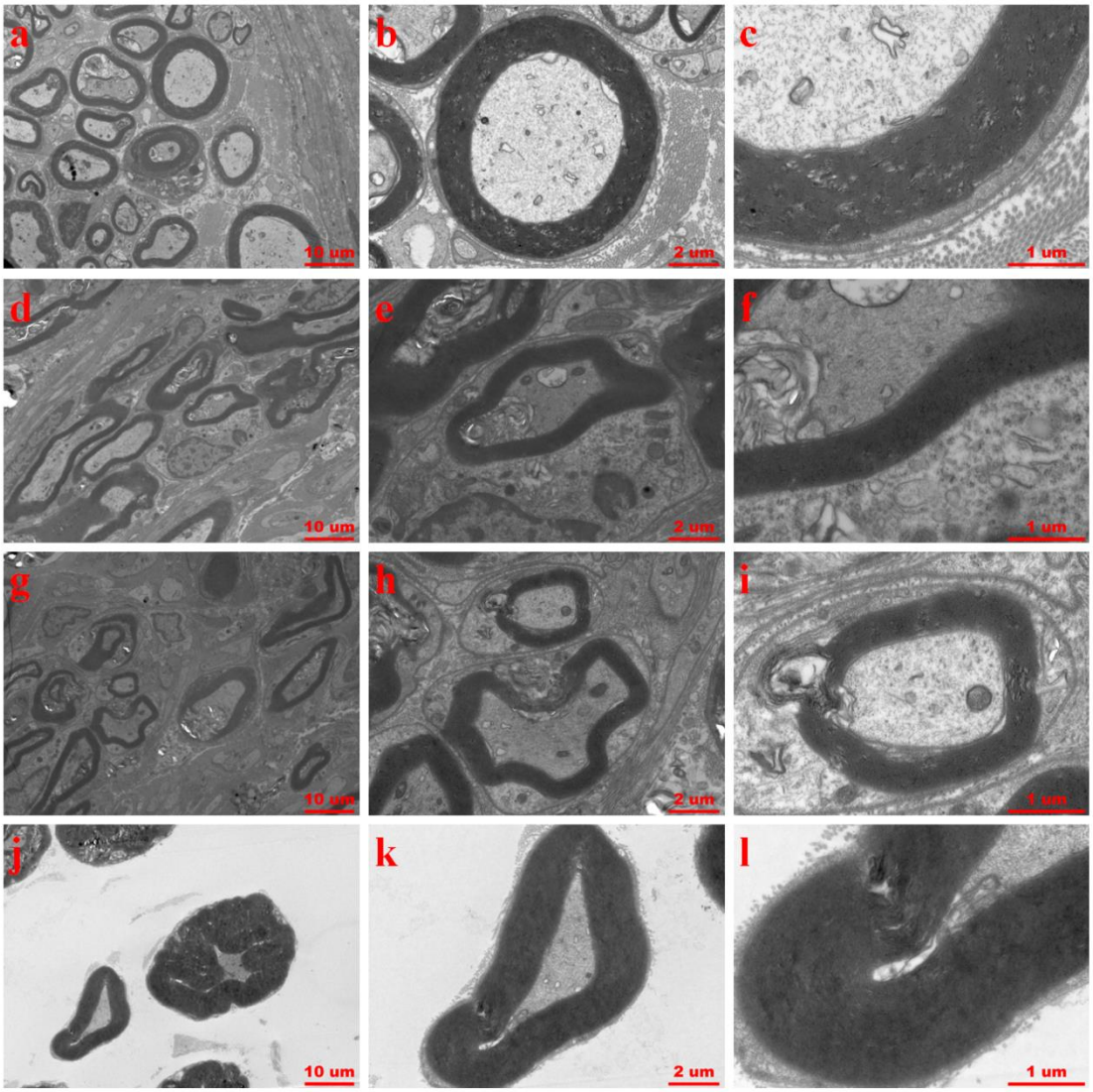

Figure S11. TEM for axonal regeneration and remyelination state at 12 weeks postoperatively. a-c) COL/NC/PCL. d-f) NC/PCL. g-i) PCL. j-l) Autograft. Scale bar = 10 μm in a, d, g, j). Scale bar = 2 μm in b, e, h, k). Scale bar = 1 μm in c, f, i, l), related to Figure 6.

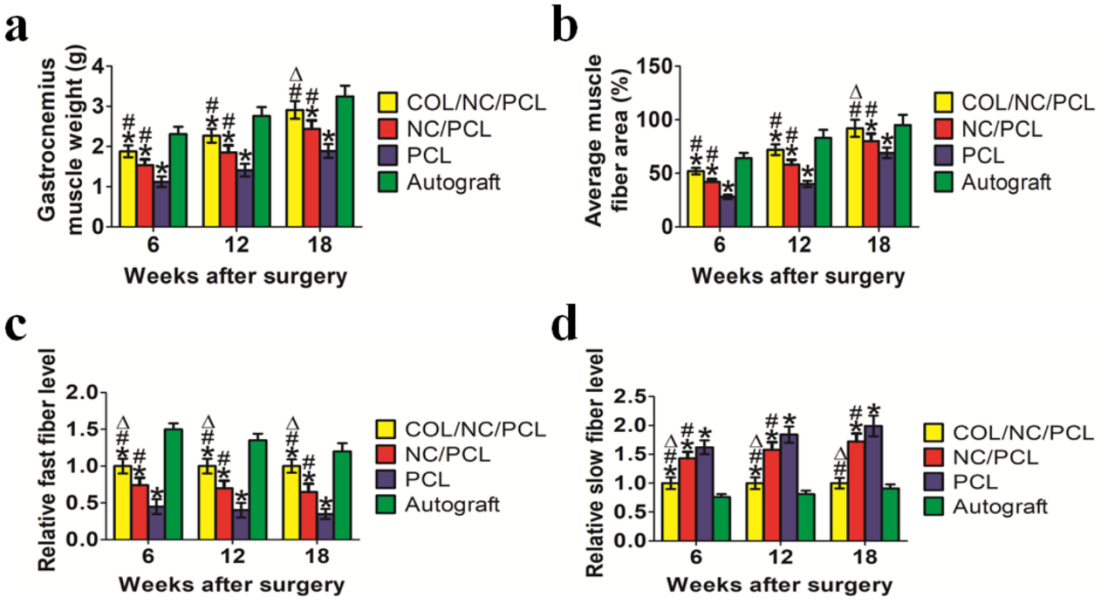

Figure S12. **Muscle viability evaluation at 6, 12 and 18 weeks after surgery.** a) Gastrocnemius muscle weight (g). b) Average muscle fiber area (%). c) Relative fast fiber level. d) Relative slow fiber level. $^{*}p<0.05$ compared with autograft, $^{\#}p<0.05$ compared with PCL, $^{\Delta}p<0.05$ compared with NC/PCL, related to Figure 6.

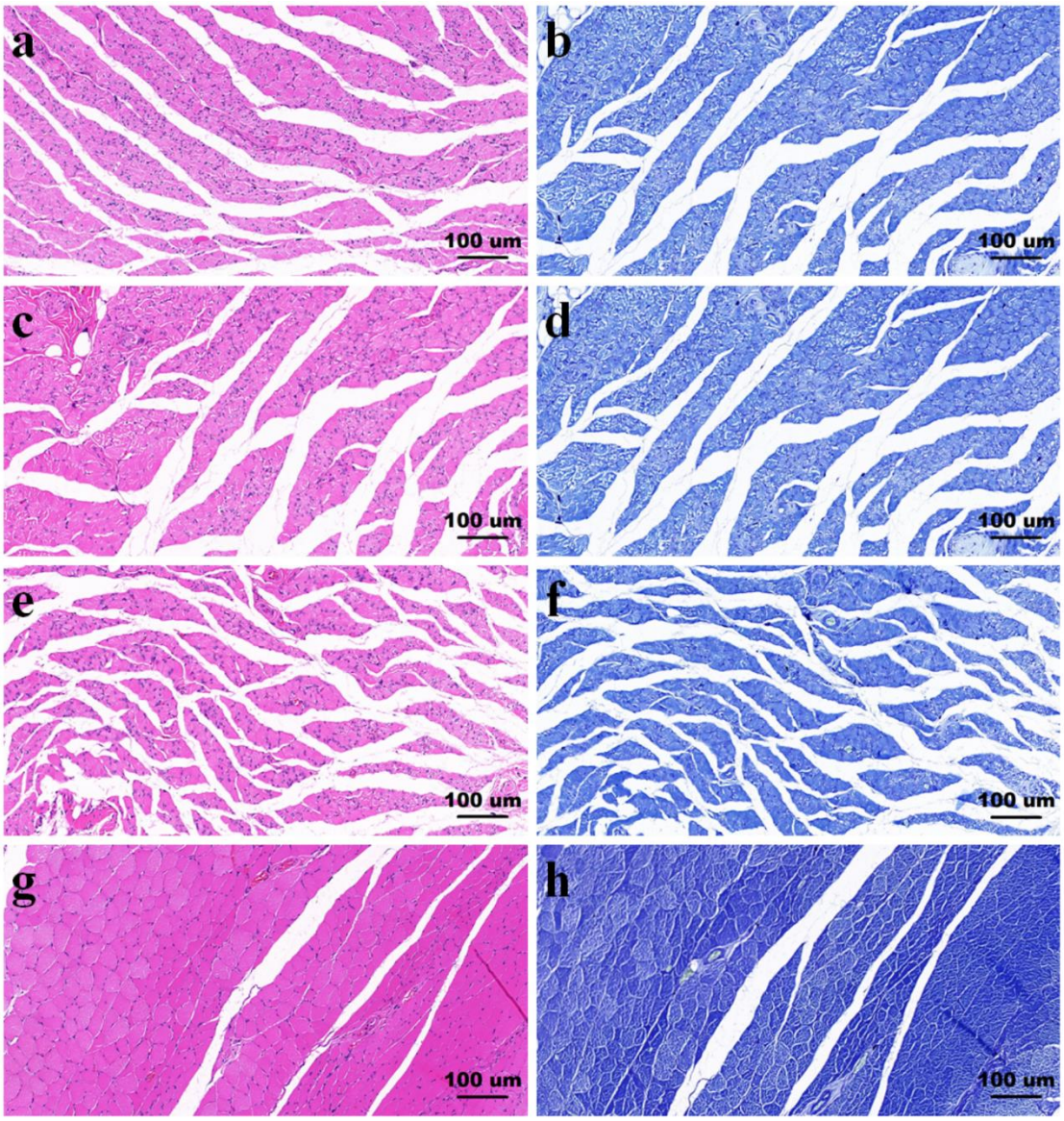

Figure S13. **HE (a, c, e, g) and TB (b, d, f, h) staining showing muscle morphology at 6 weeks postoperatively.** a, b) COL/NC/PCL. c, d) NC/PCL. e, f) PCL. g, h) Autograft. Scale bar = 100 μm, related to Figure 6.

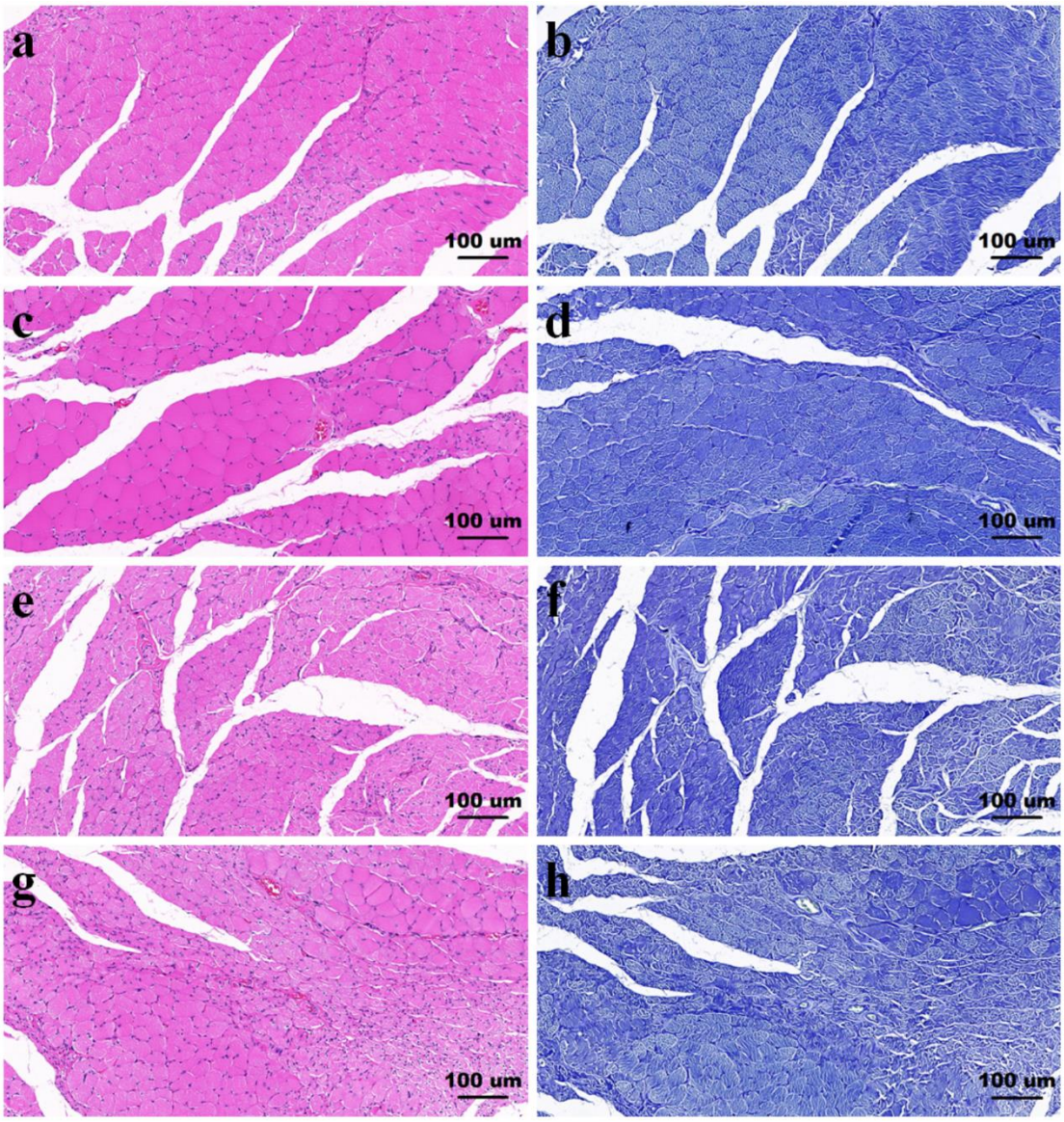

Figure S14. **HE (a, c, e, g) and TB (b, d, f, h) staining showing muscle morphology at 12 weeks postoperatively.** a, b) COL/NC/PCL. c, d) NC/PCL. e, f) PCL. g, h) Autograft. Scale bar = 100 μm, related to Figure 6.

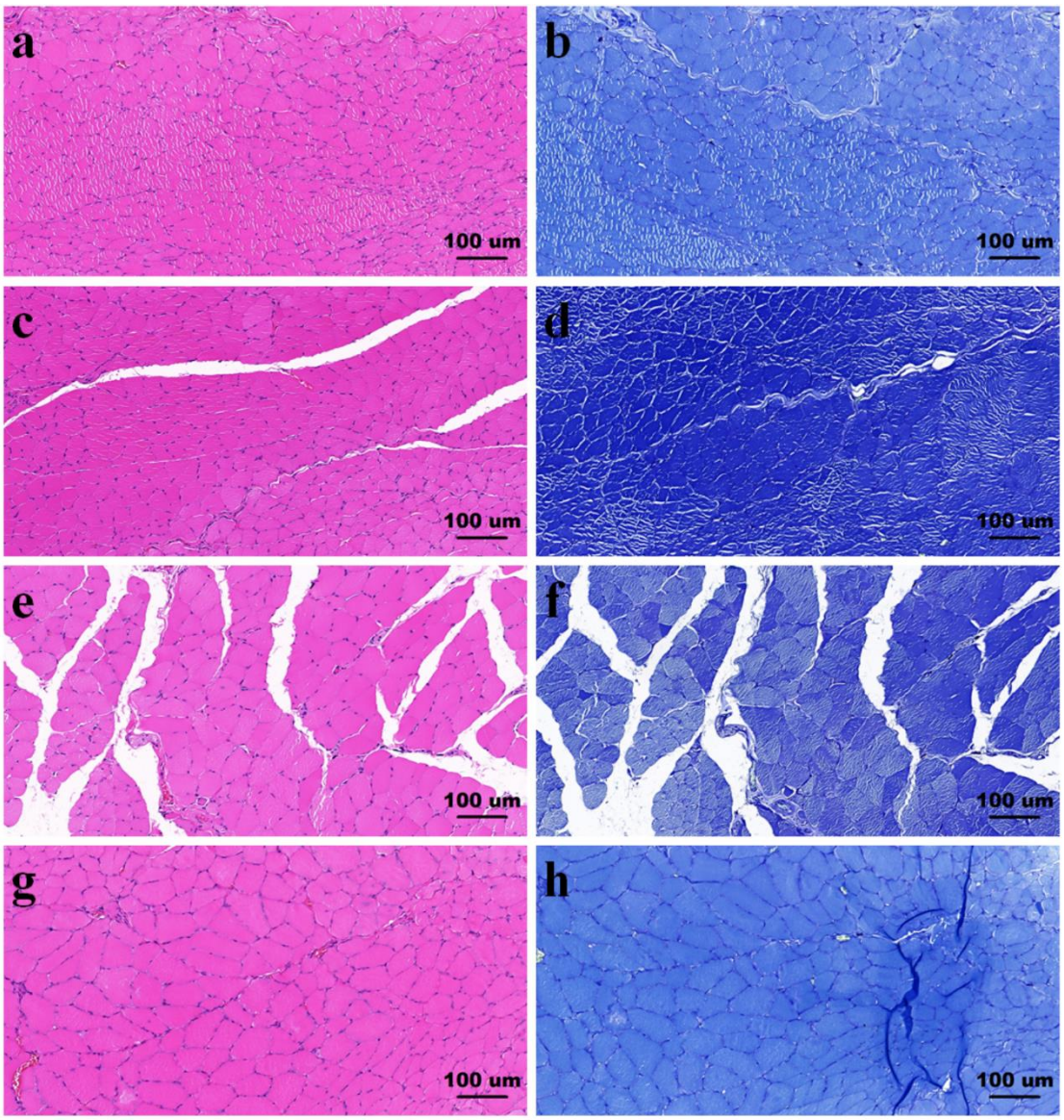

Figure S15. **HE (a, c, e, g) and TB (b, d, f, h) staining showing muscle morphology at 18 weeks postoperatively.** a, b) COL/NC/PCL. c, d) NC/PCL. e, f) PCL. g, h) Autograft. Scale bar = 100 μm, related to Figure 6.

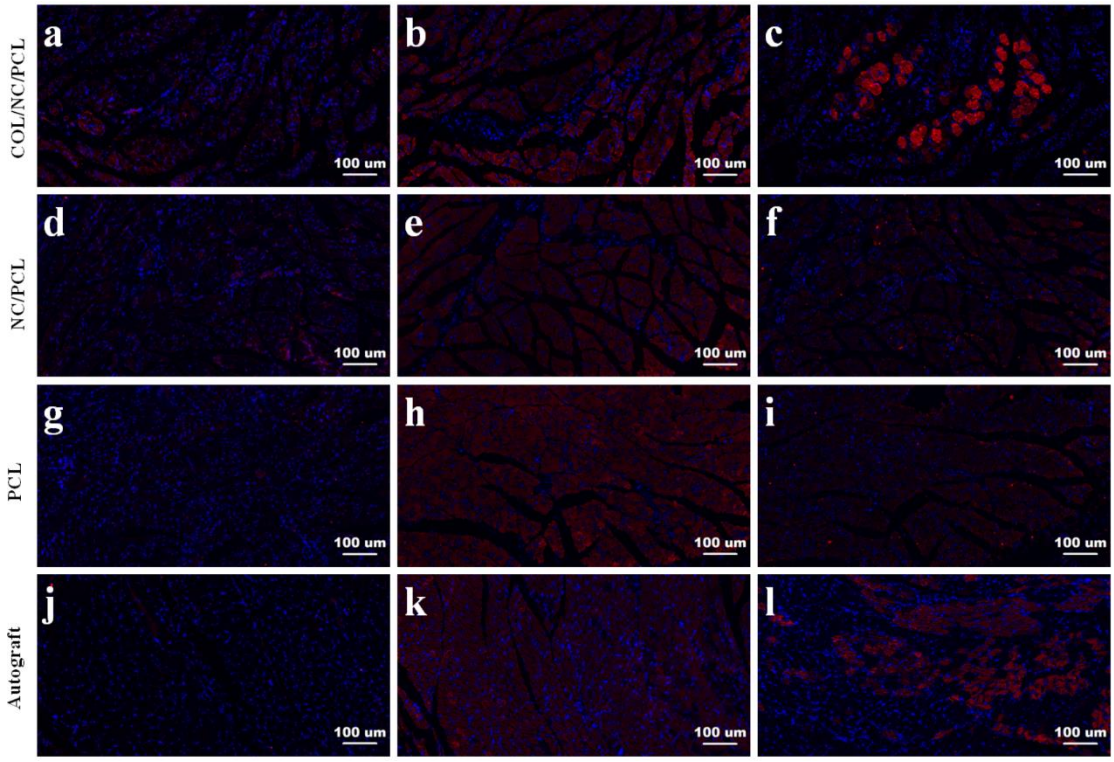

Figure S16. **Laminin (a, d, g, j), fast type myosin (b, e, h, k), slow type myosin (c, f, i, l) staining showing muscle viability at 6 weeks postoperatively.** a, b, c) COL/NC/PCL. d, e, f) NC/PCL. g, h, i) PCL. j, k, l) Autograft. Scale bar = 100 μm, related to Figure 6.

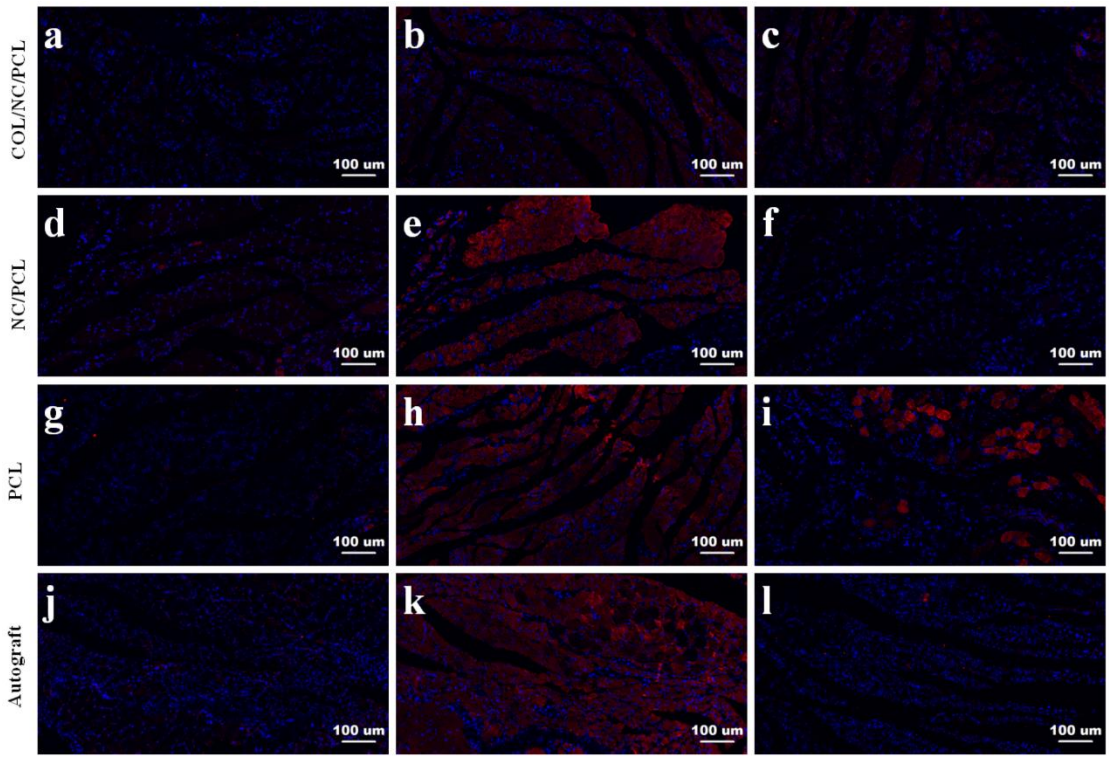

Figure S17. **Laminin (a, d, g, j), fast type myosin (b, e, h, k), slow type myosin (c, f, i, l) staining showing muscle viability at 12 weeks postoperatively.** a, b, c) COL/NC/PCL. d, e, f) NC/PCL. g, h, i) PCL. j, k, l) Autograft. Scale bar = 100 μm, related to Figure 6.

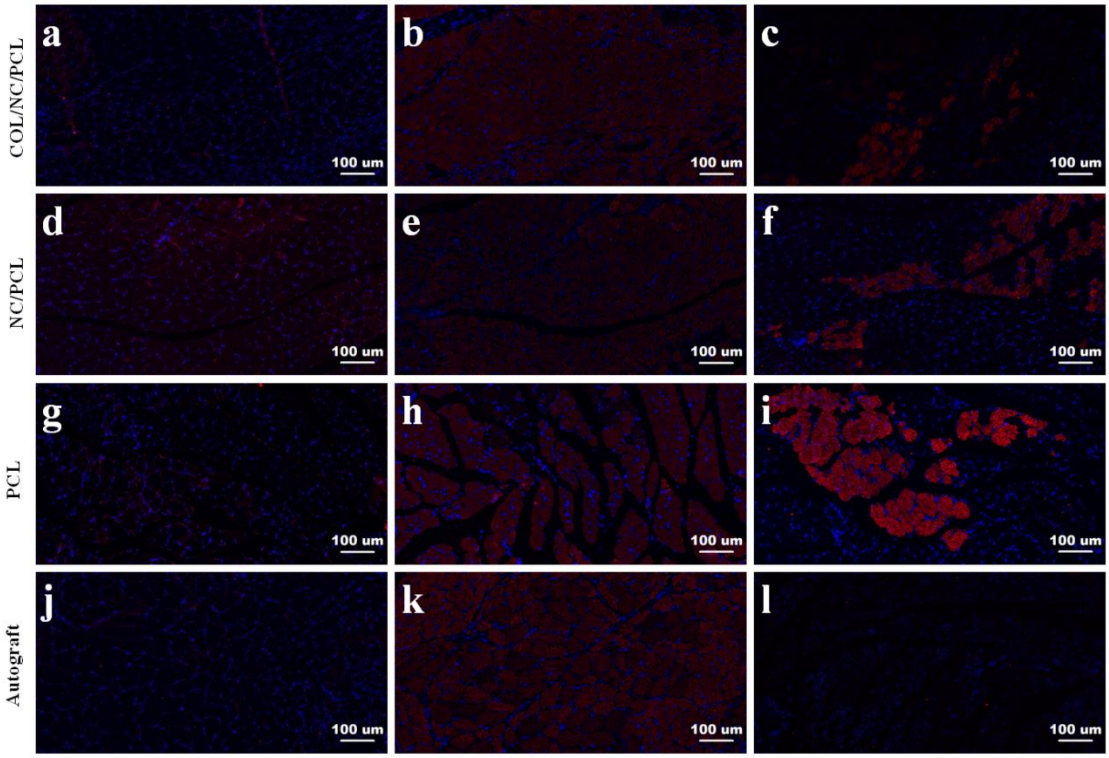

Figure S18. **Laminin (a, d, g, j), fast type myosin (b, e, h, k), slow type myosin (c, f, i, l) staining showing muscle viability at 18 weeks postoperatively.** a, b, c) COL/NC/PCL. d, e, f) NC/PCL. g, h, i) PCL. j, k, l) Autograft. Scale bar = 100 μm, related to Figure 6.

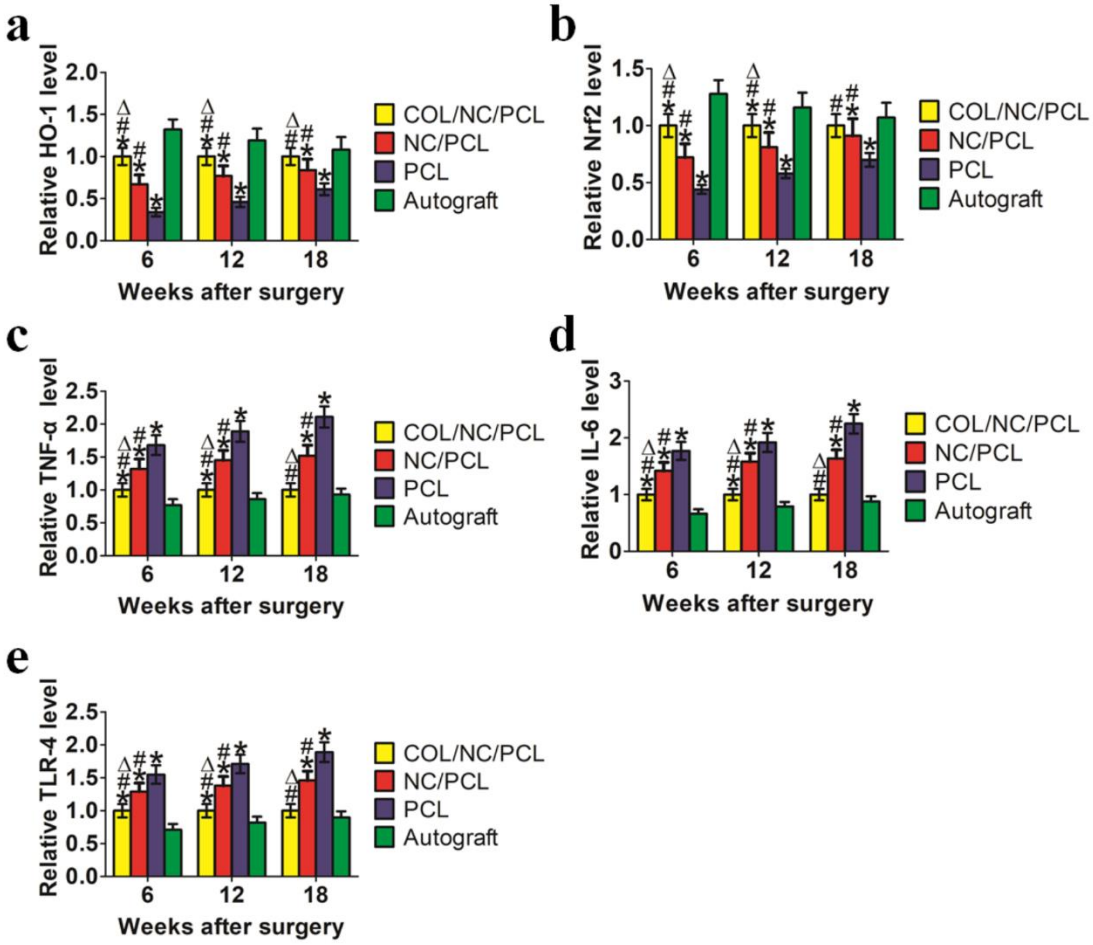

Figure S19. **Oxidative stress and inflammation state evaluation at 6, 12 and 18 weeks after surgery.** a) Relative HO-1 level. b) Relative Nrf2 level. c) Relative TNF-α level. d) Relative IL-6 level. e) Relative TLR-4 level. $^{*}p<0.05$ compared with autograft, $^{\#}p<0.05$ compared with PCL, $^{\Delta}p<0.05$ compared with NC/PCL, related to Figure 7,8.

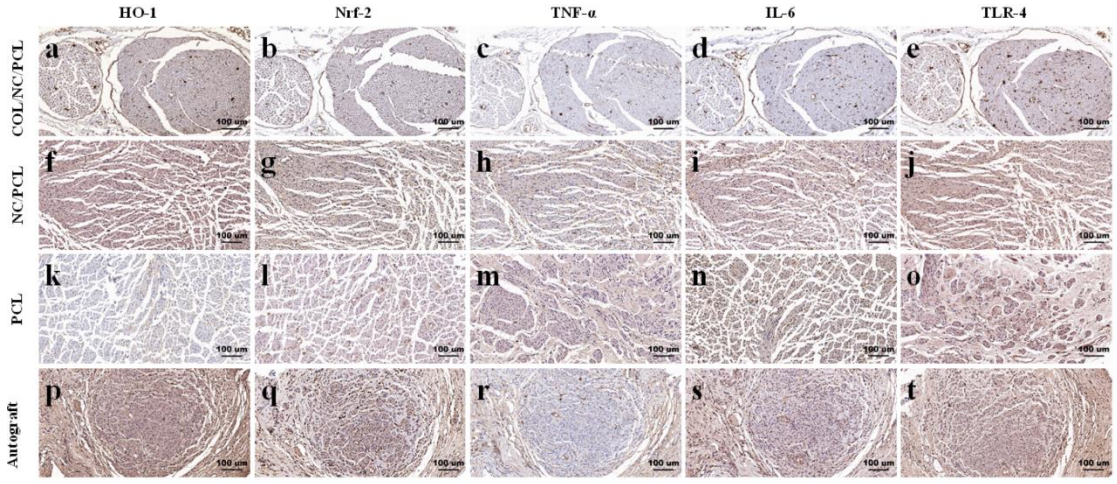

Figure S20. **HO-1 (a, f, k, p), Nrf2 (b, g, l, q), TNF-α (c, h, m, r), IL-6 (d, i, n, s), TLR-4 (e, j, o, t) staining showing oxidative stress and inflammation state of regenerated nerves at 6 weeks postoperatively.** a-e) COL/NC/PCL. f-j) NC/PCL. k-o) PCL. p-t) Autograft. Scale bar = 100 μm, related to Figure 7,8.

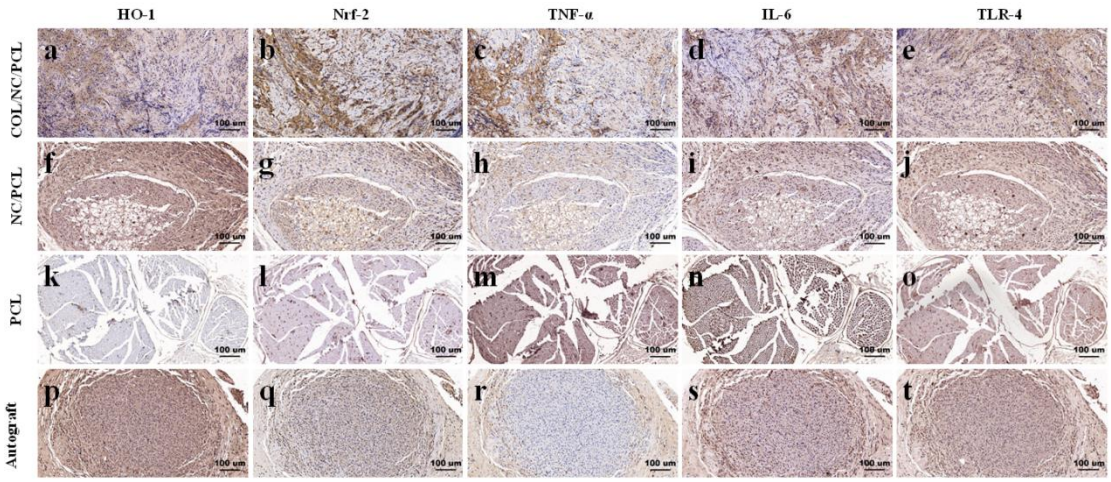

Figure S21. **HO-1 (a, f, k, p), Nrf2 (b, g, l, q), TNF-α (c, h, m, r), IL-6 (d, i, n, s), TLR-4 (e, j, o, t) staining showing oxidative stress and inflammation state of regenerated nerves at 12 weeks postoperatively.** a-e) COL/NC/PCL. f-j) NC/PCL. k-o) PCL. p-t) Autograft. Scale bar = 100 μm, related to Figure 7,8.

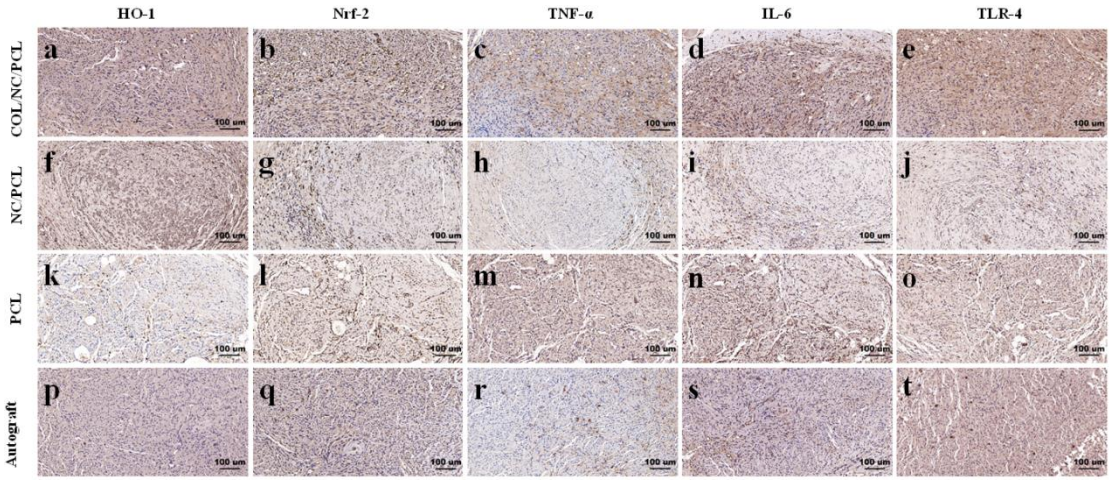

Figure S22. **HO-1 (a, f, k, p), Nrf2 (b, g, l, q), TNF-α (c, h, m, r), IL-6 (d, i, n, s), TLR-4 (e, j, o, t) staining showing oxidative stress and inflammation state of regenerated nerves at 18 weeks postoperatively.** a-e) COL/NC/PCL. f-j) NC/PCL. k-o) PCL. p-t) Autograft. Scale bar = 100 μm, related to Figure 7,8.

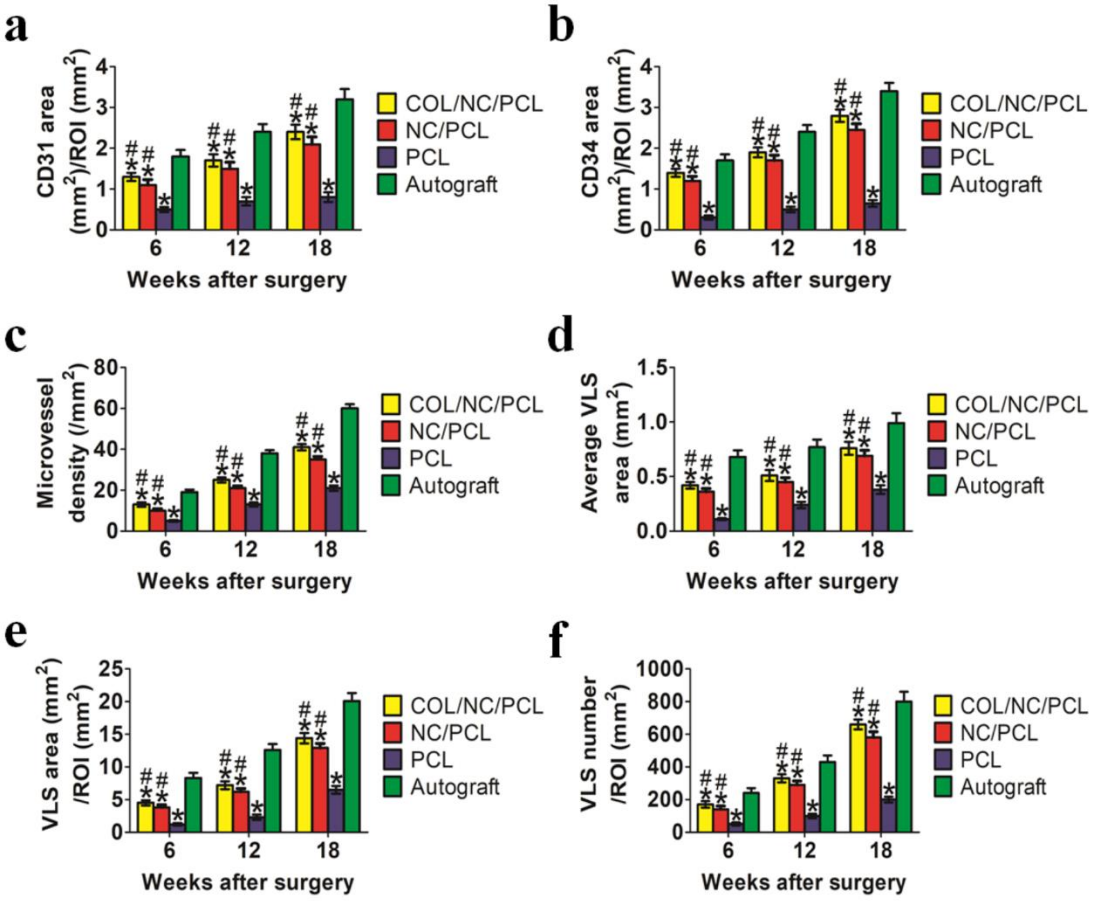

Figure S23. **Angiogenesis evaluation of regenerated nerves at 6, 12 and 18 weeks after surgery.** a) CD31 area (mm^2)/ROI (mm^2). b) CD34 area (mm^2)/ROI (mm^2). c) Microvessel density (/mm^2). d) Average VLS area (mm^2). e) VLS area (mm^2)/ ROI (mm^2). f) VLS number/ ROI (mm^2). $^{*}p<0.05$ compared with autograft, $^{\#}p<0.05$ compared with PCL, related to Figure 7,8.

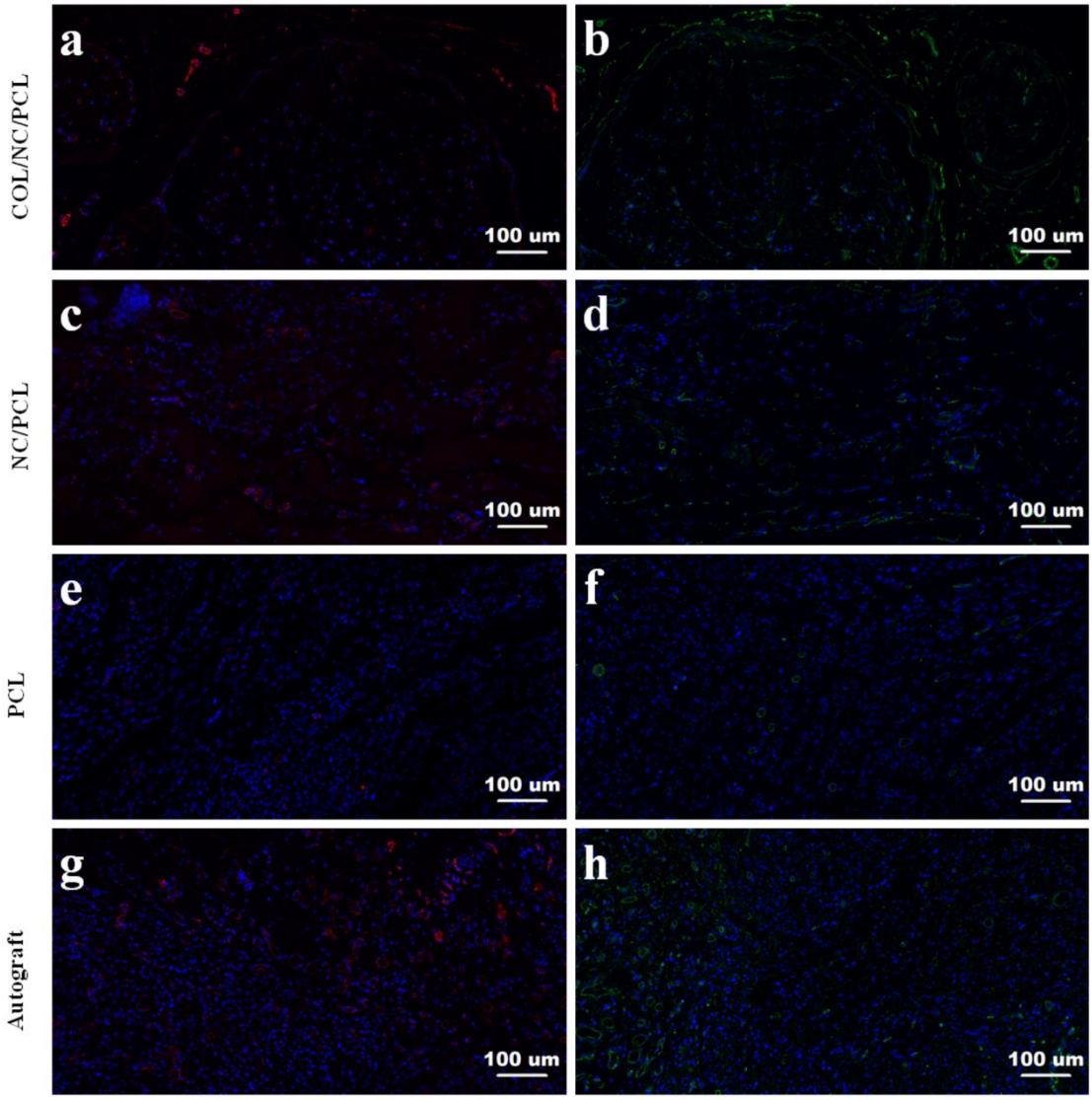

Figure S24. **CD31 (a, c, e, g) and CD34 (b, d, f, h) staining showing angiogenesis state of regenerated nerve morphology at 6 weeks postoperatively.** a, b) COL/NC/PCL. c, d) NC/PCL. e, f) PCL. g, h) Autograft. Scale bar = 100 μm, related to Figure 7,8.

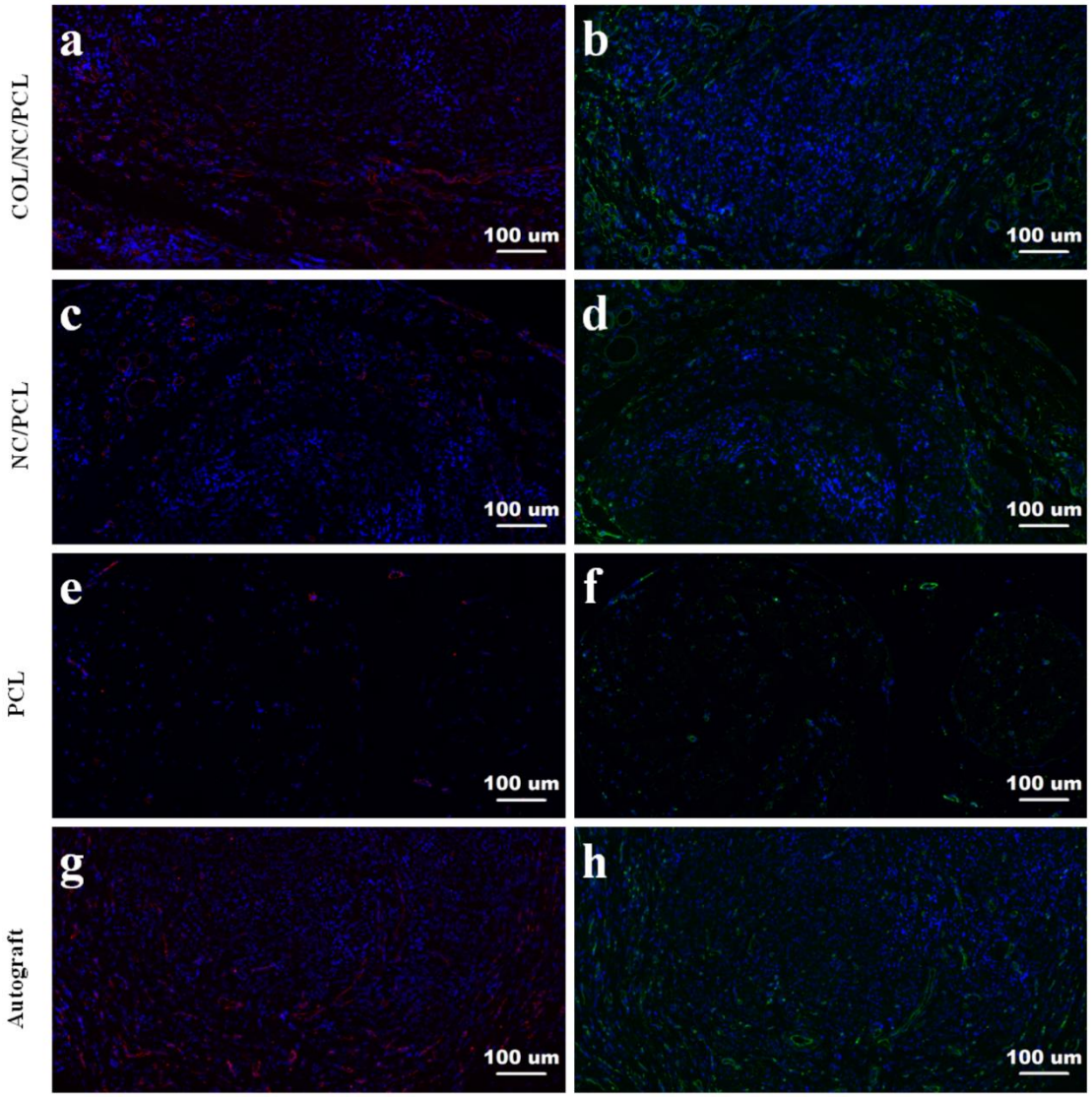

Figure S25. **CD31 (a, c, e, g) and CD34 (b, d, f, h) staining showing angiogenesis state of regenerated nerve morphology at 12 weeks postoperatively.** a, b) COL/NC/PCL. c, d) NC/PCL. e, f) PCL. g, h) Autograft. Scale bar = 100 μm, related to Figure 7,8.

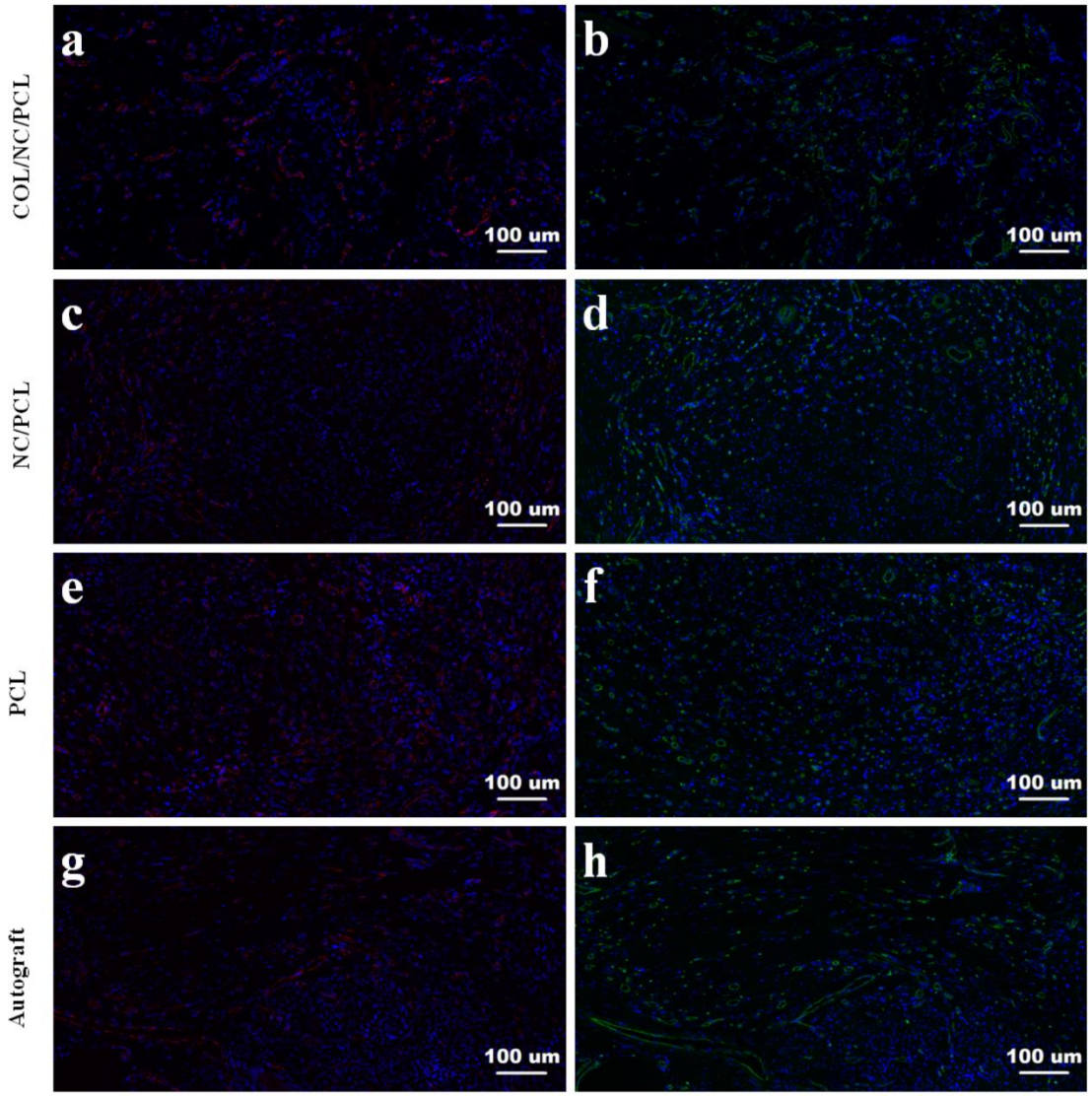

Figure S26. **CD31 (a, c, e, g) and CD34 (b, d, f, h) staining showing angiogenesis state of regenerated nerve morphology at 18 weeks postoperatively.** a, b) COL/NC/PCL. c, d) NC/PCL. e, f) PCL. g, h) Autograft. Scale bar = 100 μm, related to Figure 7,8.

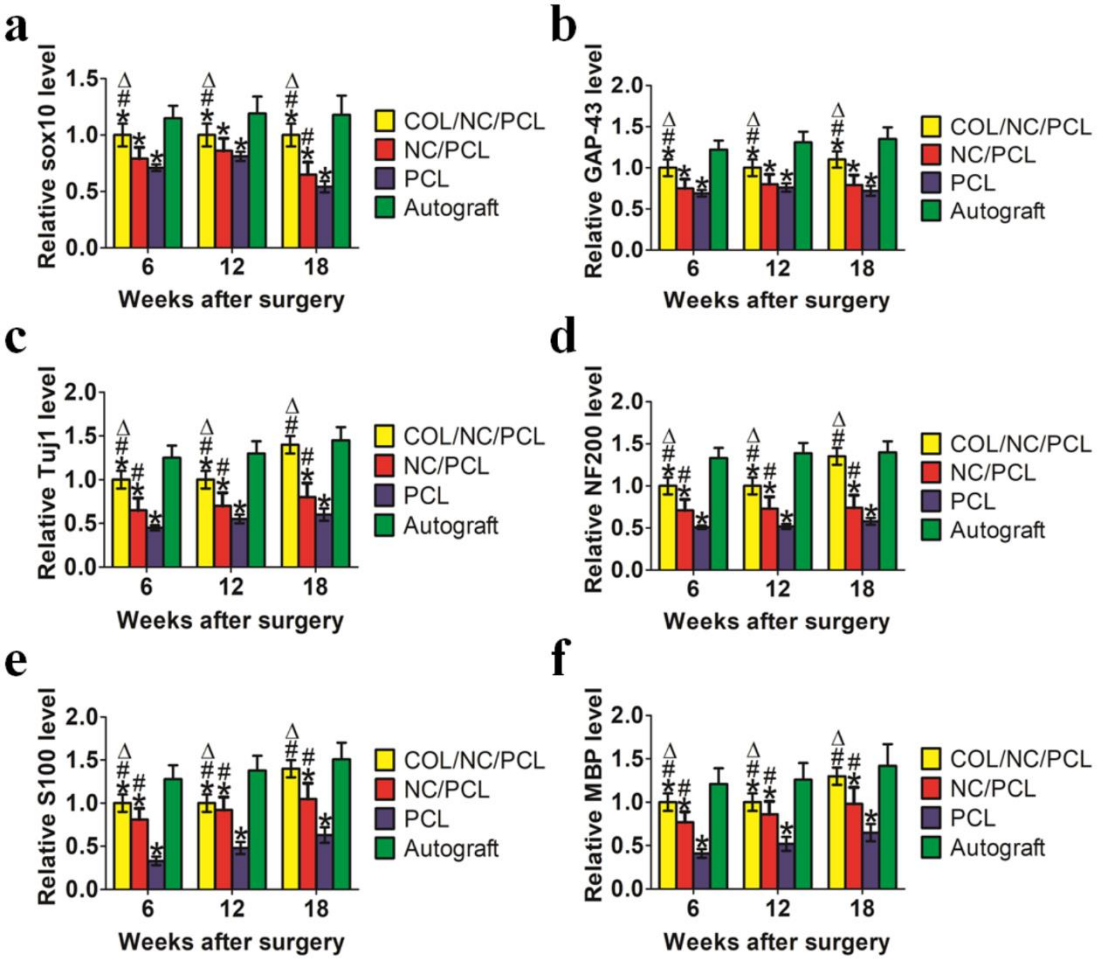

Figure S27. **Axonal regeneration and remyelination evaluation using neural markers at 6, 12 and 18 weeks after surgery.** a) Relative sox10 level. b) Relative GAP-43 level. c) Relative Tuj1 level. d) Relative NF200 level. e) Relative S100 level. f) Relative MBP level. $^{*}p<0.05$ compared with autograft, $^{\#}p<0.05$ compared with PCL, $^{\Delta}p<0.05$ compared with NC/PCL, related to Figure 7,8.

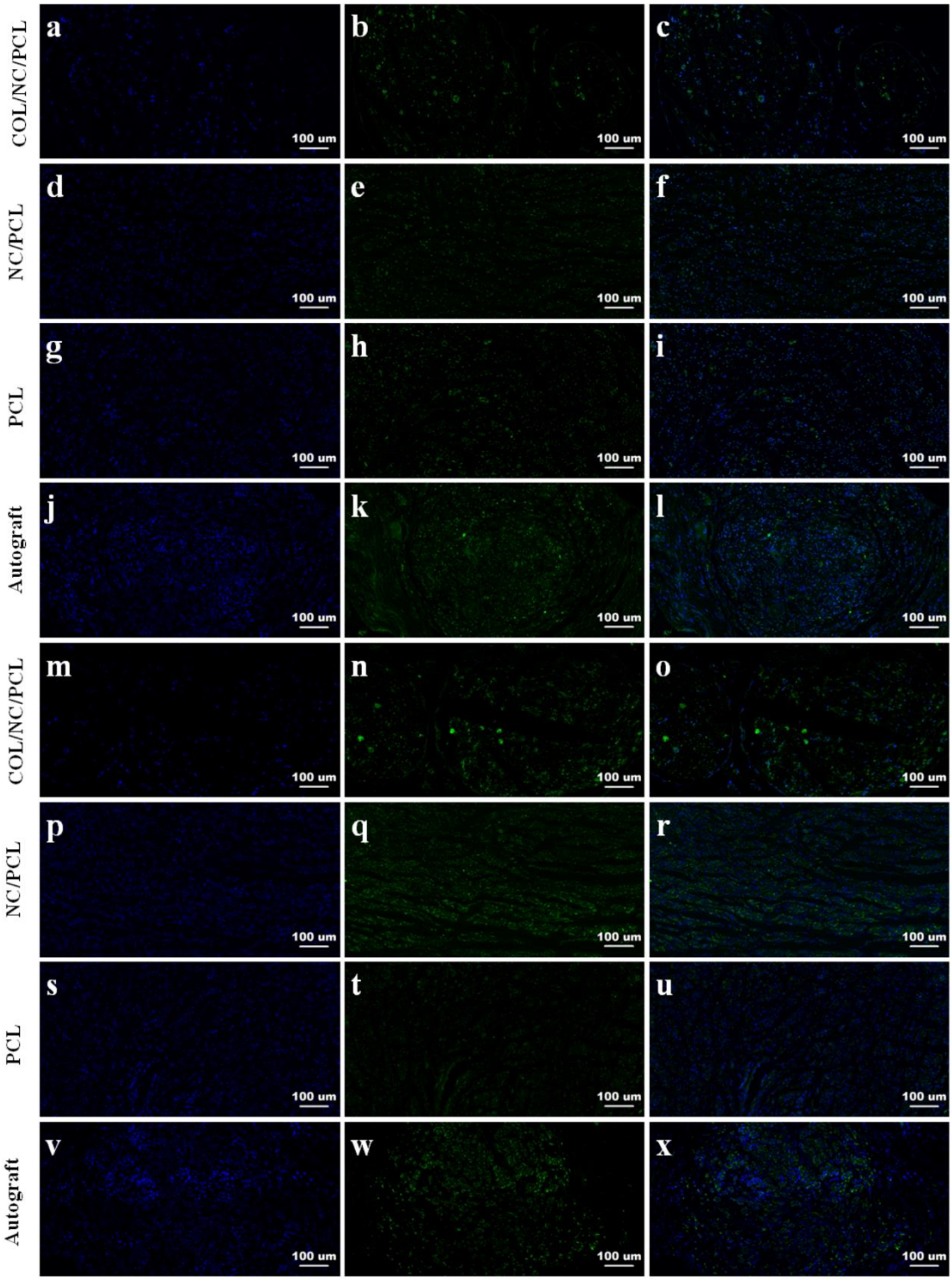

Figure S28. **Sox10 (a-l) and GAP-43 (m-x) staining showing neural viability at 6 weeks postoperatively.** a-c, m-o) COL/NC/PCL. d-f, p-r) NC/PCL. g-i, s-u) PCL. j-l, v-x) Autograft. a, d, g, j, m, p, s, v) Dapi staining. b, e, h, k) sox10 staining. n, q, t, w) GAP-43 staining. c, f, i, l, o, r, u, x) Merged images. Scale bar = 100 μm, related to Figure 7,8.

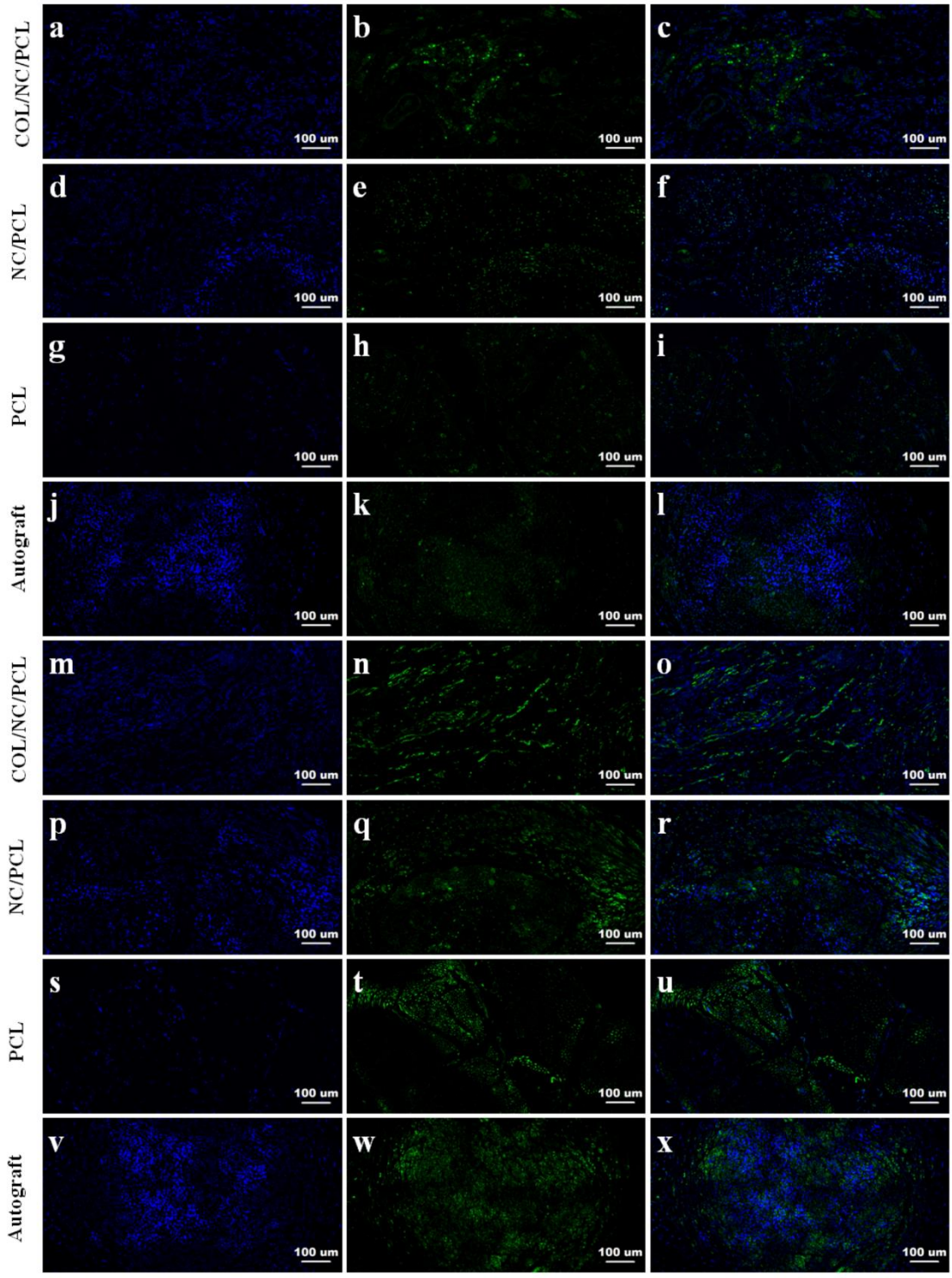

Figure S29. **Sox10 (a-l) and GAP-43 (m-x) staining showing neural viability at 12 weeks postoperatively.** a-c, m-o) COL/NC/PCL. d-f, p-r) NC/PCL. g-i, s-u) PCL. j-l, v-x) Autograft. a, d, g, j, m, p, s, v) Dapi staining. b, e, h, k) sox10 staining. n, q, t, w) GAP-43 staining. c, f, i, l, o, r, u, x) Merged images. Scale bar = 100 μm, related to Figure 7,8.

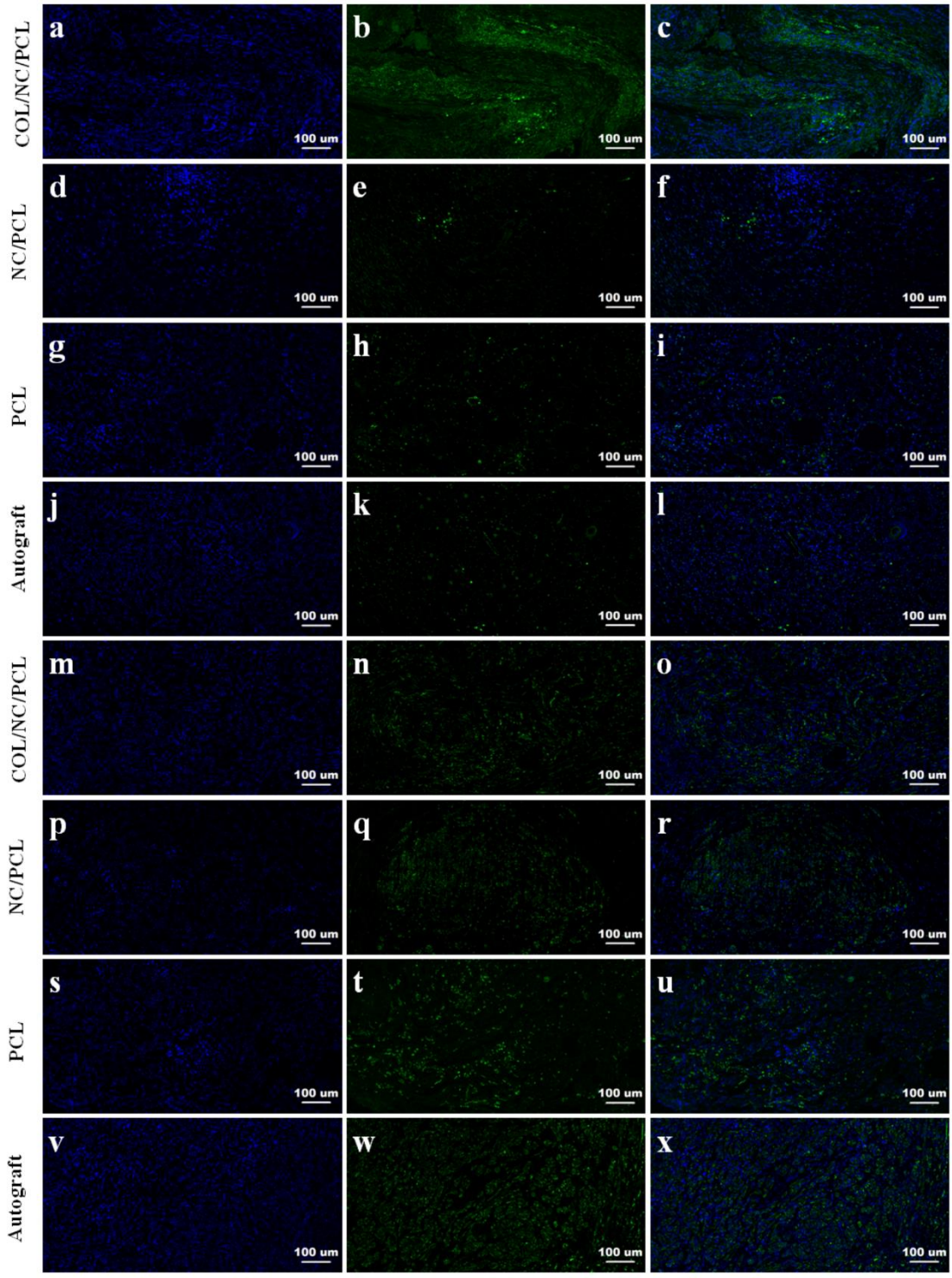

Figure S30. **Sox10 (a-l) and GAP-43 (m-x) staining showing neural viability at 18 weeks postoperatively.** a-c, m-o) COL/NC/PCL. d-f, p-r) NC/PCL. g-i, s-u) PCL. j-l, v-x) Autograft. a, d, g, j, m, p, s, v) Dapi staining. b, e, h, k) sox10 staining. n, q, t, w) GAP-43 staining. c, f, i, l, o, r, u, x) Merged images. Scale bar = 100 μm, related to Figure 7,8.

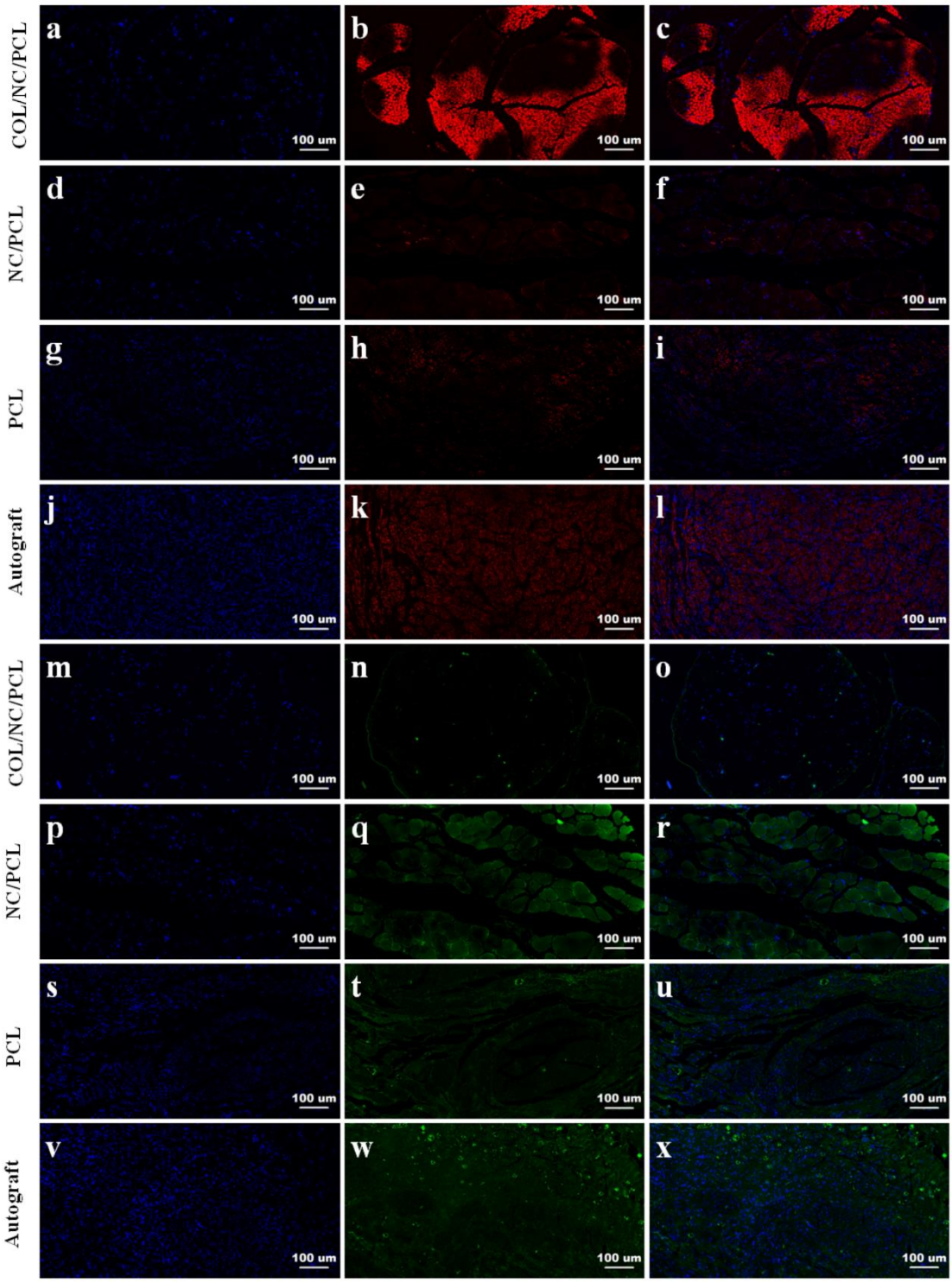

Figure S31. **MBP (a-l) and S100 (m-x) staining showing Schwann cell viability and remyelination at 6 weeks postoperatively.** a-c, m-o) COL/NC/PCL. d-f, p-r) NC/PCL. g-i, s-u) PCL. j-l, v-x) Autograft. a, d, g, j, m, p, s, v) Dapi staining. b, e, h, k) MBP staining. n, q, t, w) S100 staining. c, f, i, l, o, r, u, x) Merged images. Scale bar = 100 μm, related to Figure 7,8.

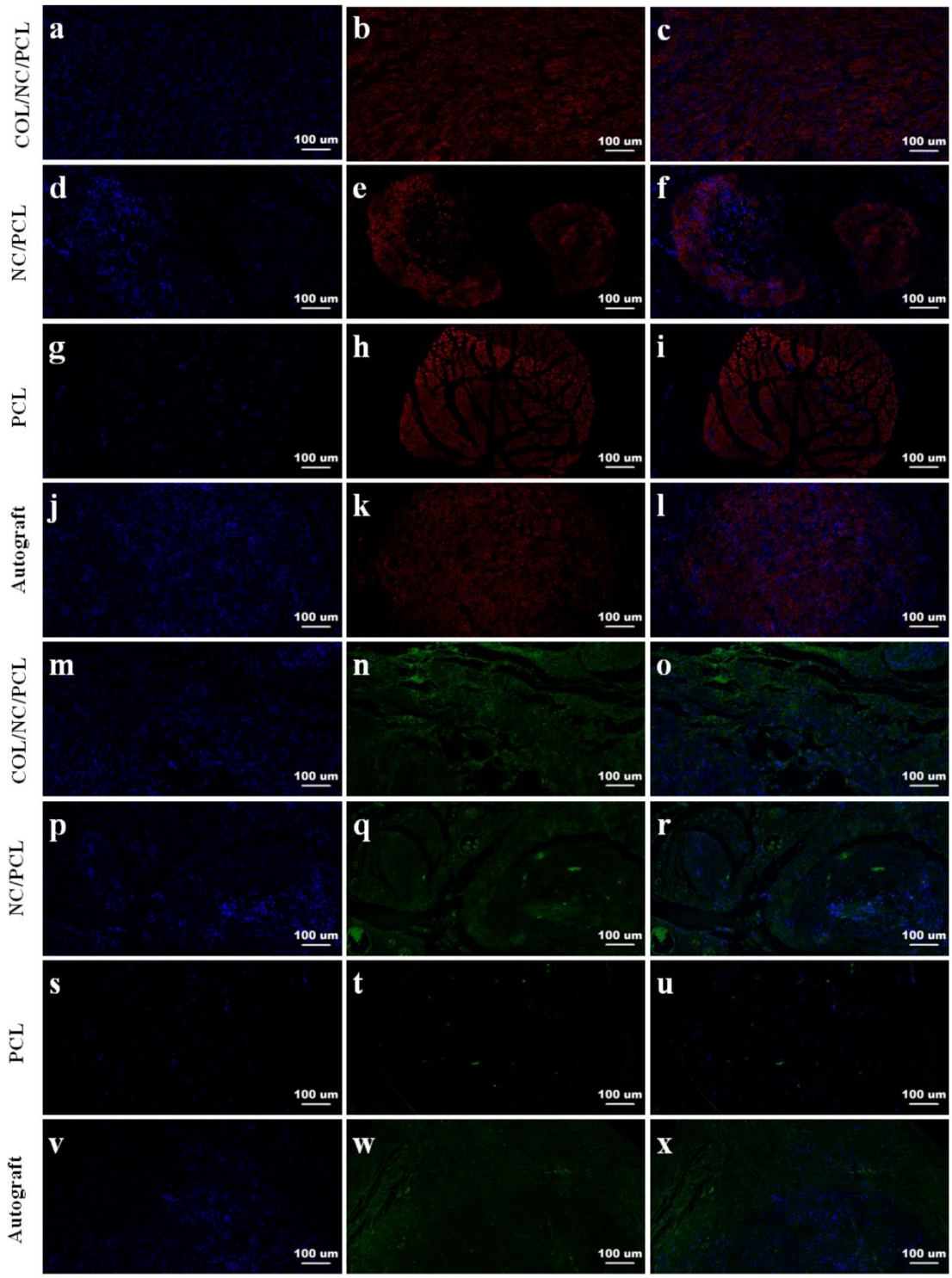

Figure S32. **MBP (a-l) and S100 (m-x) staining showing Schwann cell viability and remyelination at 12 weeks postoperatively.** a-c, m-o) COL/NC/PCL. d-f, p-r) NC/PCL. g-i, s-u) PCL. j-l, v-x) Autograft. a, d, g, j, m, p, s, v) Dapi staining. b, e, h, k) MBP staining. n, q, t, w) S100 staining. c, f, i, l, o, r, u, x) Merged images. Scale bar = 100 μm, related to Figure 7,8.

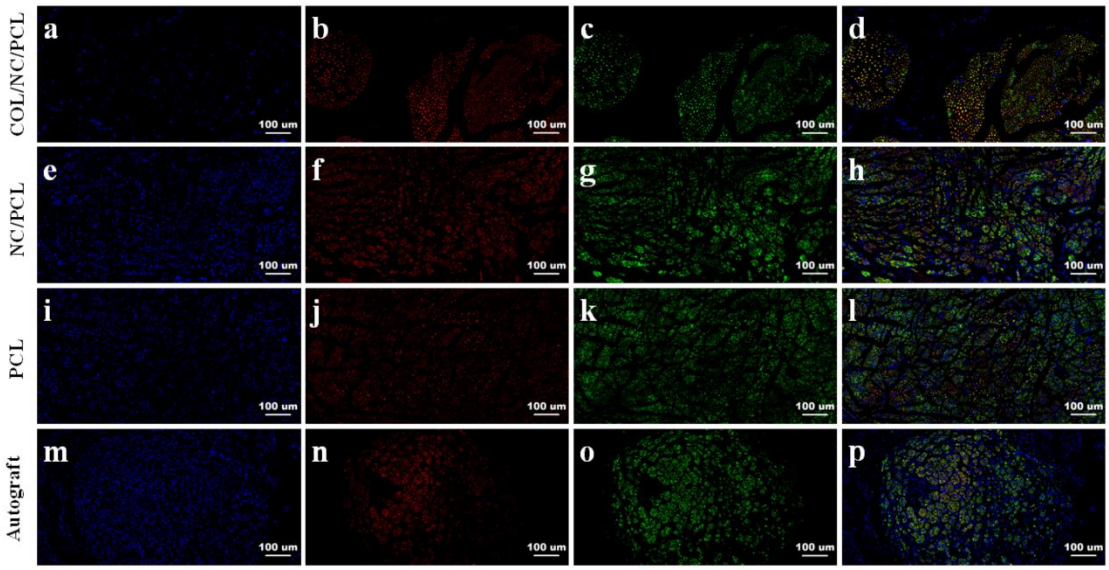

Figure S33. **Triple immunofluorescence of regenerated nerve tissues showing axonal restoration at 6 weeks postoperatively.** a-d) COL/NC/PCL. e-h) NC/PCL. i-l) PCL. m-p) Autograft. a, e, i, m) Dapi staining. b, f, j, n) NF200 staining. c, g, k, o) Tuj1 staining. d, h, l, p) Merged images. Scale bar = 100 μm, related to Figure 7,8.

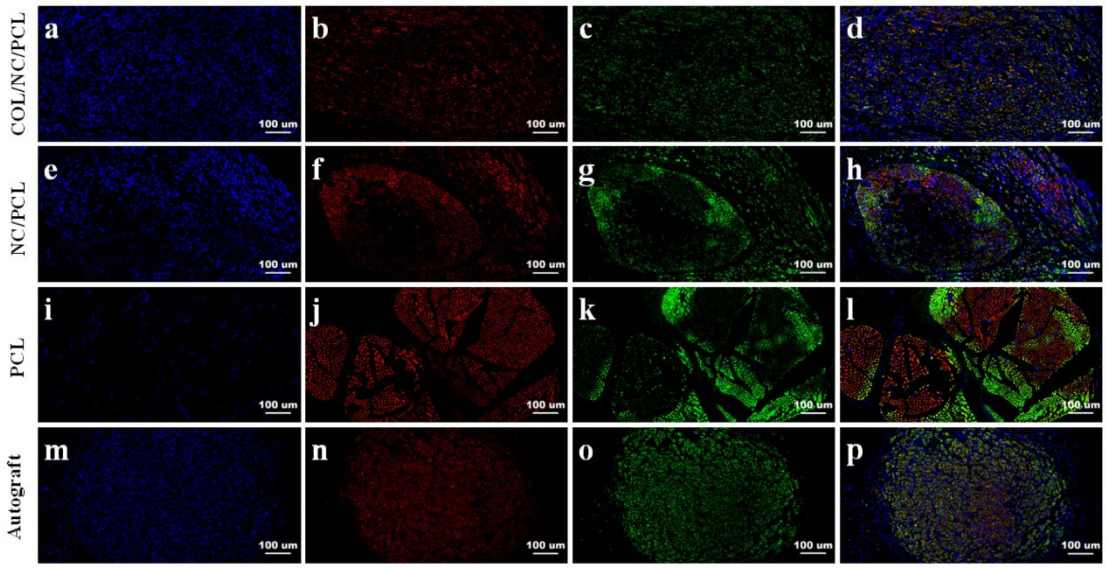

Figure S34. **Triple immunofluorescence of regenerated nerve tissues showing axonal restoration at 12 weeks postoperatively.** a-d) COL/NC/PCL. e-h) NC/PCL. i-l) PCL. m-p) Autograft. a, e, i, m) Dapi staining. b, f, j, n) NF200 staining. c, g, k, o) Tuj1 staining. d, h, l, p) Merged images. Scale bar = 100 μm, related to Figure 7,8.

Transparent Methods

Preparation and characterization for COL/NC/PCL nerve conduit

Nanoceria and collagen were purchased from Sigma Aldrich (USA). PCL was purchased from Pertorp UK Limited Inc. We used an intelligent toward-target sprayer in the fabrication of 3D COL/NC/PCL nerve conduit. We separately dissolved nanoceria and PCL with dichloromethane in the tube-shaped mold. We set the NC/PCL in a drying flat board and created a film structure. The conduit was composed of three layers: the innermost layer-NC/PCL mixed layer, the outermost layer-COL layer and the middle layer-PCL layer. A tube mold was rolling counterclockwise, under a sprayer that injected different solution layer by layer crosslinked by dichloromethane on the rolling tube. Finally, after the conduit was solid, we removed the microneedles and the rolling tubular mold.

We evaluated the outermost and innermost surface morphology using SEM. We prepared ultrathin slides of COL/NC/PCL conduit coated by gold for 1 minute, followed by SEM observation (VEGA3 XMU, Czech and Sirion 200, USA). These images were taken at 2000×, 5000× and 10000× at an accelerating voltage of 5kV and 10 kV. We evaluated the nanoceria morphology using transmission electron microscope (TEM, Talos F200X, China). We randomly chose representative images for final assessment. We measured the conduit thickness, calculated the surface elastic modulus by nanoindentation (Nano Indenter G200, Agilent, USA) and atomic force microscope (AFM, Dimension Icon & FastScan Bio, USA), and measured the elastic recovery curves. All material characterization experiments were performed at Instrumental Analysis Center of SJTU. The anti-oxidant condition was evaluated by Total Antioxidant Capacity Assay Kit (Sigma, USA). We analyzed the concentration and efficacy of nanoceria by measuring the reduction of Cu^{2+} to Cu^{+}.

Cell viability and morphology assays

RSCs were purchased from the cell bank of the Chinese Academy of Sciences (Shanghai, China). RSCs were cultured in high-glucose Dulbecco's modified Eagle's medium supplemented with 15% fetal bovine serum (Gibco, USA). Cells were cultured in 5% CO_2 incubator at 37℃. We sterilized COL/NC/PCL and other conduits by ultraviolet exposure for 4 hours. In order to evaluate the biocompatibility of COL/NC/PCL and NC/PCL conduits to determine their appropriate concentration for neural growth, we compared 0.5%, 1%, 2% to 4% nanoceria in different conduits using cell counting kit 8 (CCK8) assay at 6, 12 and 24 hours. Cell proliferation assay was also performed using CCK8 at 24h, 72h, 120h and 168h. Cells were seeded in different conduits at 2×10^{4} cm^{-2}. The medium from each conduit was evaluated for the absorbance at a wavelength of 450 nm was determined using a multifunctional microplate reader (Thermo Fischer Scientific 3001, USA).

RSCs were cultured in COL/NC/PCL, NC/PCL and PCL conduit for two days at 4×10^{4} cm^{-2}. We then washed cells by PBS and fixed them with 2.5% glutaraldehyde at 4℃ overnight. 1% osmium tetroxide was used as a secondary fixation for 1 hour followed by graded ethanol dehydration from 50% to 100% for 30 minutes. The samples were dried for 4 hours after addition of hexamethyldisilazane (Sigma Aldrich, USA). Finally, we observed these sample via SEM (VEGA3 TESCAN). In addition, we also performed phalloidin immunofluorescent staining to observe actin filament. RSCs were were fixed by 4% paraformaldehyde for 1 hour and washed by PBS. Then, FITC-Phalloidin (Abcam, USA) working solution stained cells for 30 minutes. All

samples were washed with PBS for three times. Then, cell nuclei were stained with DAPI (1:500, Gibco, USA). We observed these samples via a confocal immunofluorescence microscope (Leica, Germany).

Immunofluorescent assays

After culturing for two days on scaffolds, RSCs were fixed in 4% paraformaldehyde for 1 hour and immersed in 0.1% Triton X-100 (Sigma Aldrich) for 10 minutes. Then, they were incubated with primary antibodies overnight at 4℃ and secondary antibodies at for 2 hours at 25℃. In addition, we stained cell nuclei with 4,6-diamidino-2 phenylindole (DAPI) (1:500, Gibco, USA). The primary antibodies were anti-GFAP (1:1000, Abcam, USA), anti-Ki67 (1:250, Abcam, USA), anti-Tuj1 (1:500, Abcam, USA), anti-S100 beta (1:100, Abcam, USA) and anti-MBP (1;200, Abcam, USA). The secondary antibody was Alexa Fluor 488-conjugated mouse anti-rabbit IgG (1:250, Abcam, USA). We observed samples using a confocal immunofluorescence microscope (Leica, Germany).

Flow cytometry (FCM), western blotting and quantitative PCR

We used 2', 7'-dichlorofluorescein diacetate (DCFDA) measurement (beyotime, China) to evaluate oxidative stress state. RSCs were incubated with 15 μmol/L DCFDA solution, and cultured for 1 hour in 5% CO_2 incubator at 37℃. Then cells were washed with PBS for three times followed by FCM evaluation.

For Western Blotting, we lysed RSCs in RIPA buffer to collect total proteins, conducted sodium dodecyl sulfate polyacrylamide gel electrophoresis (SDS-PAGE) and transferred samples onto polyvinylidene fluoride (PVDF) sheet. The samples were incubated at 4℃ overnight with the following primary antibodies: anti-Ki67 (1:5000, Abcam, USA), anti-Tuj1 (1:1000, Abcam, USA), anti-MBP (1:2000, Abcam, USA), anti-S100 beta (1:5000, Abcam, USA), anti-HO-1 (1:5000, Abcam, USA), anti-MnSOD (1:10000, Abcam, USA), anti-GCLC (1:3000, Gibco, USA) and anti-IL-6 (1:5000, Gibco, USA). To further quantify the results, we extracted total RNA from the cells using TRIzol reagent (Thermo Fisher, USA) according to the manufacturer's protocol. RNA was reverse-transcribed into cDNA with PrimeScriptTM (Takara) in RNA-free water. According to the manufacturer's instructions, samples were run on a real-time PCR biosystem. The primer sequences (forward 5'-3') were as follows, HO-1: TTAAGCTGGTGATGGCCTCC; MnSOD: CACCGAGGAGAAGTACCACG; GCLC: TACCGAGGCTACGTGTCAGA; IL-6: CCCAACTTCCAATGCTCTCCT; Ki67: ACAGGGCTTAGGAAACAGTCC; Tuj1: AGCTCACCCAGCAGATGTTC; S100: CGATGCCCCGGAAAGTTAGA; MBP: TGGGAAACCACTCTGGAAAG.

Animal surgery

We chose sixty SD rats (male, weighing 150-160g) in this experiment. They were randomly allocated into 4 groups, COL/NC/PCL conduit group, NC/PCL conduit group, PCL conduit group and autograft group and were evaluated at 6, 12 and 18 weeks postoperatively. All animals were housed in the specific pathogen-free environment. 50 mg kg^{-1} pentobarbital sodium was injected peritoneally to guarantee satisfactory anesthesia. We sterilized operative regions, exposed skins, muscles and eventually the sciatic nerve. A 15-mm-long nerve was removed and two nerve ends were reconnected by different 15-mm conduits and autografts.

Later, we sutured muscles and skins layer by layer. All animals received penicillin injection for one week. Observations and procedures were performed at 6, 12 and 18 weeks respectively. Animal care and use were authorized by the Animal Ethics Committee for Shanghai Jiao Tong University (SJTU, No. A2017072).

Functional assays

Walking track analysis was performed to evaluate motor activity, including some variables, like the distance between the first toe and the fifth toe (TS), the third toe to the heal (PL), and the second toe to the fourth toe (IT). We compared experimental legs (E) and normal legs (N) at the same time and followed the formula, SFI = (−38.3 × (EPL − NPL)/NPL) + (109.5 × (ETS − NTS)/NTS) + (13.3 × (EIT − NIT)/NIT) − 8.8. Higher SFI value indicates better function. We performed mass weighing of the gastrocnemius muscle of the experimental sides via a digital scale (Sartorius, Germany).In addition to motor evaluation, sensory performance was performed as follows. We measured withdrawal latency using paw withdrawal apparatus (Ugo Basile Inc.). We used a quarter of the maximal heat for 0.1 seconds, with a 10-minute interval. Then, we recorded the results with our rats standing on all four paws.

Electrophysiological assays

We performed electrophysiological assays on the experimental rats at 6, 12 and 18 weeks postoperatively. Under satisfactory anesthesia, we exposed the right sciatic nerve and placed bipolar electrodes at two nerve ends to transmit single electrical signal. In addition, we recorded electromyography (EMG) by fixing an electrode at gastrocnemius muscle. Latency and distance between nerve ends under stimulation was measured and used for calculating NCV and DCMAP.

Nerve and muscle morphology assays

We dissected 15-mm regenerated nerves after electrophysiological assays by removing conduits outside. Nerves were prepared as ultra-thin 3-μm-thick sections. We performed HE, TB staining and TEM to evaluate nerve microstructure. We evaluated several indicators for peripheral nerve regeneration, including number of myelinated axons, thickness of myelin sheath, regenerated axon area, and average myelinated axon diameter. The gastrocnemius muscle of the experimental leg was subjected to HE and TB staining. Random fields of view were used for evaluating muscle fibers. The muscle was evaluated by the Average muscle fiber area (Avm) according to the formula: Avm = Am/At × 100%. Am represents the area of muscle fibers. At represents the total area of the field.

Immunofluorescent assays

We harvested nerve and muscle samples at 6, 12 and 18 weeks postoperatively. Frozen samples were stained using the following primary antibodies: anti-slow myosin heavy chain (1:500, Abcam, USA), anti-fast myosin heavy chain (1:500, Abcam, USA), anti-laminin (1:300, Abcam, USA), anti-CD31(1:500, Abcam, USA), anti-CD34 (1:500, Abcam, USA), anti-VEGF (1:500, Abcam, USA), anti-HO-1 (1:500, Abcam, USA), anti-IL-6 (1:400, Abcam, USA), anti-Nrf2 (1:200, Abcam, USA), anti-TLR4 (1:500, Abcam), anti-TNF-α (1:300, Abcam, USA), anti-sox10 (1:250, Abcam, USA), anti-GAP-43 (1:250, Abcam, USA), anti-Tuj1 (1:100, Abcam, USA), anti-NF200 (1:250, Abcam, USA), anti-S100 beta (1:500, Abcam, USA), and anti-MBP (1:200, Abcam, USA). The

slides were observed under an immunofluorescence microscope (Leica, USA).

Statistical analysis

All tests were repeated thrice and results were displayed as mean ± standard deviation. A p value of 0.05 was considered significant by one-way analysis of variance (ANOVA).